

Near-Earth Asteroid Characterization and Observation (NEACO) Mission to Asteroid (469219) 2016 HO₃

Chandranth Venigalla,* Nicola Baresi,[†] Jonathan D. Aziz,[†] Benjamin Bercovici,[†]
Daniel N. Brack,[†] Andrew Dahir,[†] Stijn De Smet,[†] JoAnna Fulton,[†] Marielle M. Pellegrino,[†] and
Stefaan Van wal[†]

University of Colorado at Boulder, Boulder, Colorado 80309

DOI: 10.2514/1.A34268

The Near-Earth Asteroid Characterization and Observation (NEACO) mission is a concept study proposing to explore the fast-rotating asteroid (469219) 2016 HO₃, one of Earth's few quasi-satellites. In this study, a SmallSat spacecraft performs a scientific investigation that characterizes the asteroid at a sufficient degree to enable future, more in-depth missions. The 166 kg NEACO spacecraft uses a low-thrust, solar electric propulsion system to reach HO₃ within 22 months from launch. Its instrument suite consists of two optical cameras, two spectrometers, an altimeter, and a low-velocity impactor. Upon arrival at HO₃, NEACO uses pulsed plasma thrusters to hover at varying altitudes to enable lit surface mapping, shape modeling, and surface spectroscopy. The spacecraft will then perform several flybys to estimate the asteroid's mass. Finally, NEACO releases a low-velocity impactor during very low-altitude hovering to validate the existence of regolith and estimate the magnitude of surface cohesion. The science operations are completed within 8 months and the total mission is completed in less than 3 years. The NEACO mission concept integrates novel small-body analyses and proximity operation techniques with high-technology-readiness-level spacecraft components to achieve its science objectives within a reasonable mission timeline.

Nomenclature

a	=	semimajor axis
B	=	mass-to-cross-sectional-area ratio of the spacecraft
C_r	=	coefficient of reflectivity
c	=	speed of light
D	=	dark current
D_T	=	asteroid diameter
F	=	flux from HO ₃ , Jy
F_0	=	reference flux, Jy
f	=	photon rate, photons/s
G	=	slope parameter
m_v	=	apparent visual magnitude
N_r	=	read noise
R	=	distance between the spacecraft and HO ₃ , AU
$R_{\odot,b}$	=	distance between the sun and HO ₃ , AU
r	=	spacecraft distance from asteroid
$\mathbf{r}_{b,\odot}$	=	position vector of HO ₃ with respect to the sun
\mathbf{r}	=	relative position vector of the spacecraft as seen from HO ₃
S'	=	pulsating synodic reference frame
S/N	=	signal-to-noise ratio
$\mathcal{U}(\mathbf{r})$	=	gravitational potential of HO ₃
\mathbf{u}	=	applied thrust
β	=	solar radiation pressure parameter
Δ	=	line-of-sight drift over exposure time, m
μ_{\odot}	=	gravitational parameter of the sun
χ	=	angle between the HO ₃ -sun and HO ₃ -spacecraft lines
ϕ	=	telescope diameter, m

Φ_{\odot}	=	solar irradiance
ω_D	=	spacecraft angular rotation rate, rad/s
ω_T	=	asteroid angular rotation rate, rad/s

I. Introduction

THE recently discovered asteroid (469219) 2016 HO₃ is Earth's closest known quasi-satellite, with a heliocentric orbit that keeps the object between 38 and 100 lunar distances (0.10–0.26 AU) from our planet. HO₃ is predicted to maintain this behavior for at least an additional 300 years, making it the most stable quasi-satellite currently tracked. These two properties have earned HO₃ much interest as a candidate target for future in situ exploration missions [1]. Studying and characterizing the small-body population within the neighborhood of Earth is critical to understanding the threat of near-Earth asteroids. Accordingly, several national and international efforts aim to discover and track these objects, as well as to investigate their physical nature [2]. Characterizing the physical composition and orbital behavior of HO₃ may inform how this asteroid population was formed and increase understanding of these threatening objects. Additionally, entities with interest in in situ resource use may similarly consider HO₃ a desirable candidate. The prospect of a manned or unmanned in situ exploration of the asteroid using only current knowledge of the body presents several challenges, due to the large uncertainties on the asteroid composition and surface properties. A low-cost preliminary survey mission would provide invaluable data to better prepare a more elaborate in situ operation in the future. This provides the motivation for the Near-Earth Asteroid Characterization and Observation (NEACO) concept study to design a SmallSat mission to asteroid (469219) 2016 HO₃.

The NEACO mission concept is specifically designed to maximize the scientific data return from HO₃ with a launch mass less than 180 kg. The 180 kg limit allows a C_3 of up to 25 km²/s² when using the Vega launcher. Further, 180 kg is the payload limit for an Evolved Expendable Launch Vehicle (EELV) Secondary Payload Adapter (ESPA) ring, and thus would allow a similar mission to make use of a shared launch instead of a dedicated launch. The NEACO spacecraft is a 166 kg SmallSat that implements a low-thrust, solar electric propulsion system to reach its target in less than 2 years. Its instrument suite includes a narrow-angle optical camera, a medium-resolution optical camera, two spectrometers, a laser altimeter, and a low-velocity impactor. Upon arrival at HO₃, NEACO uses pulsed plasma thrusters to hover, first at a high altitude of 45 km to perform lit

Received 12 June 2018; revision received 27 November 2018; accepted for publication 10 December 2018; published online 31 January 2019. Copyright © 2018 by Chandranth Venigalla, Nicola Baresi, Jonathan D. Aziz, Benjamin Bercovici, Daniel N. Brack, Andrew Dahir, Stijn De Smet, JoAnna Fulton, Marielle M. Pellegrino, and Stefaan Van wal. Published by the American Institute of Aeronautics and Astronautics, Inc., with permission. All requests for copying and permission to reprint should be submitted to CCC at www.copyright.com; employ the eISSN 1533-6794 to initiate your request. See also AIAA Rights and Permissions www.aiaa.org/randp.

*Ph.D. Student, Smead Department of Aerospace Engineering Sciences 431 UCB; chve1854@colorado.edu.

[†]Ph.D. Student, Smead Department of Aerospace Engineering Sciences 431 UCB.

surface mapping and shape modeling, and subsequently at a lower altitude of 10 km to refine these models and perform surface spectroscopy. Following the hovering phases, the spacecraft performs several flybys with decreasing periaapses in order to estimate the asteroid's mass. Finally, NEACO uses an additional flyby to release a low-velocity impactor to validate the existence of regolith and estimate the magnitude of surface cohesion. The science operations are completed within 8 months and the total mission is completed in less than 3 years. The NEACO mission concept integrates novel small-body analyses and proximity operation techniques with high-technology-readiness-level (TRL) spacecraft components to achieve the science objectives within a reasonable mission timeline.

This paper is organized as follows. First, the science objectives of the mission are motivated and defined using the Science Traceability Matrix method. Following this, a general overview of the mission concept is presented to outline the design of the mission operations and spacecraft bus. The selected launch, cruise trajectory, arrival, and science observation phases are presented sequentially through the mission timeline. Each aspect of the spacecraft design is then outlined, detailing the instrument suite and spacecraft bus component specifications and capabilities. The second half of the paper is dedicated to a detailed analysis of the key technical challenges of achieving a successful mission to the target asteroid HO₃, and how the novel solutions presented by the NEACO mission concept are developed. These include development of the low-thrust trajectory, acquisition of the substantially dim target for guidance and navigation, and understanding the complex relative dynamics between the small body and spacecraft under influence from solar gravity and solar radiation pressure such that proximity operations can be planned. Additionally, gravity estimation of the small body required implementation of a novel, multiply flyby planning method. The instrument selection process is also outlined, and the attitude determination and control system is analyzed to verify that pointing requirements are met. Finally, a method for measuring the asteroid's cohesive strength using a low-velocity impactor is presented. These details are provided to further develop the novel choices presented in the mission design and to provide insight and lessons learned for the highly challenging problem of small-body exploration in SmallSat design constraints.

Note that the mission operations and spacecraft bus have been engineered specifically with respect to how key mission challenges impact the overall design. The central question that is addressed in this paper is how the "key mission analyses" presented in the second half of this paper all come together to inform a full mission concept design. The baseline concept takes into account the analyses of the second half of the paper in order to show that a mission is feasible, but more engineering work on the mission operations planning and spacecraft bus would be required for a real mission to HO₃.

The following assumptions regarding the orbital and characteristic properties of HO₃ are implemented in the analysis of this paper. The heliocentric orbit of HO₃ is defined by JPL Horizons. The volume, spin period, and spectral type of the asteroid are defined by estimations made through current observation data [3]. The asteroid has a spherical shape with a diameter of 50 m, the spin period is approximately 28 minutes, and the spectral type is assumed to be L-type. The spin axis remains unknown. The density of the asteroid is currently unknown, and so a range of 2–5 g/cm³ with a nominal density of 3 g/cm³ is assumed. Therefore the gravitational parameter μ is assumed to be in the range of 0.009–0.022 m³/s² with a nominal value of 0.013 m³/s² based on the estimated diameter and density ranges of the asteroid.

II. Science Objectives

A. Science Objectives and Priorities

The NEACO mission concept's high-level goal is to conduct an investigation of asteroid 2016 HO₃ in order to obtain the body's defining characteristics, as a precursor to more advanced future missions. To achieve this, a set of science objectives is identified that ensures a comprehensive survey of the asteroid. Fundamental questions regarding the asteroid size, shape, composition, and surface environment are addressed by these goals, as listed in Table 1, and have associated priorities assigned by the team.

Table 1 Priority ranking of science objectives for the NEACO mission concept

Science goal deliverable	Mission priority
1. Mass estimate	High/threshold
2. Volume estimate	High/threshold
3. Global shape model	High/threshold
4. Lit surface map	High/threshold
5. High-resolution map of 1 region	Mid/baseline
6. Spectral properties	Mid/baseline
7. Surface strength	Low/extended

Threshold mission goals define the minimum set of achievements necessary for mission success. They relate to the measurement of elementary asteroid properties whose values must be known within reasonable accuracy in order to allow for the design and planning of more in-depth missions to asteroid HO₃. More specifically, knowledge of the asteroid mass, volume, and shape is required for accurate spacecraft orbit design, in particular when performing proximity operations. Maps of the asteroid surface significantly increase the feasibility of autonomous spacecraft operation, for example, by enabling on-board localization techniques. At a higher level, the asteroid's low mass and fast rotation rate result in a type of dynamical environment that has never been visited before. Given the asteroid's proximity to Earth, an exploration of its elementary characteristics may provide invaluable insight into impact threat mitigation and possible resource extraction methods. The *baseline* mission goals identify deliverables that further enhance the asteroid investigation. The high-resolution mapping of a select surface region will provide details on HO₃'s small features, which provide constraints on future missions that plan to operate on the asteroid's surface. Additionally, investigation of the body's spectral properties provides details on its composition that significantly complement a simple density estimate provided by the threshold-level goals. Finally, the surface strength characterization is designated as an *extended* mission goal, due to its higher operational risk. Nevertheless, the strength measurement validates the existence of regolith particles on super-fast rotators and places constraints on the interaction properties of these particles. Spectroscopy of the subsurface, which may be exposed by strength-measuring techniques, would further complement the baseline-level investigation of the asteroid composition.

B. Science Traceability Matrix

A science traceability matrix (STM) is used to ensure NEACO's instrument suite and mission plan will be able to meet or exceed the science goals presented in Table 1. The STM is provided in Fig. 1, where each row provides a brief but comprehensive overview of which instruments will be used to address the science and required measurements, and what the corresponding functional objectives on the instruments are. The STM also includes the resulting data products of the mission design, as a final verification that all mission requirements are met. The measurement requirements are defined by consultation from parties interested in HO₃ exploration [4], and are within reasonable expectation. To meet all of the threshold, baseline, and extended mission goals, NEACO is equipped with an altimeter, optical cameras, spectrometers, and an impactor assembly.

III. Mission Concept

A. Launch, Low-Thrust Transfer, and Arrival

The NEACO trajectory includes a dedicated launch and low-thrust transfer that reaches the sun-HO₃ L_1 point in 665 days. A mass of 144.95 kg is delivered to HO₃ with a spacecraft wet mass of 165.55 kg. The trajectory is visualized in Fig. 2 using the General Mission Analysis Tool (GMAT) [5]. Earth departure corresponds to the ArianeSpace Vega performance from Guiana Space Center, with a -5.2° declination, $C_3 = 25.0$ km²/s², and a nominal launch date of June 5, 2025. A 15-day coast is enforced postlaunch, during which the solar electric propulsion (SEP) and subsystems are tested. Thrusting with an 8 cm XiPS SEP engine begins a continuous-thrust

	Science Objectives	Measurement Objectives	Measurement Requirements	Instrument	Instrument Functional Requirements	Instrument Projected Performance	Mission Functional Requirements	Data Product
Interior and Shape	What is HO ₃ 's composition and density?	mass	10% accuracy	radio comms			5 flybys, 10 day flyby sequence	mass estimate of HO3
		volume	10% accuracy	optical camera	0.85 m/pixel	0.7 m/pixel at 45 km altitude, 1024 pixel square sensor	execute imaging sequence within 6 months	volume estimate of HO3
	How was HO ₃ formed?	shape	5 m global accuracy	optical camera	5 m/pixel	0.7 m/pixel at 45 km altitude, 1024 pixel square sensor	execute imaging sequence within 6 months	100% coverage shape model, 0.7 m resolution
Surface Characterization	What are the surface features of HO ₃ ?	lit surface map	1 m ² resolution	optical camera	1 m/pixel	0.7 m/pixel at 45 km altitude, 1024 pixel square sensor	execute imaging sequence within 6 months	surface map with 100% coverage at 0.49 m ² resolution
		high resolution lit surface map	at least one 10 m ² region at 1 cm ² resolution	optical camera	1 cm/pixel	1 mm/pixel with 1024 pixel square sensor at 600 m altitude	2 images at or below 600 m	surface map of 178 m ² region at 1 mm ² resolution
	What is HO ₃ 's surface composition?	strength	impact the surface and observe the regolith shedding	impactor	impact surface at 1 m/s	1 kg object impacting at 1 m/s	release assembly & guarantee impact	
				optical camera	1 cm/pixel	1 mm/pixel with 1024 pixel square sensor at 600 m altitude	identify impact zone, estimate impact size using before/after opt. images	1+ optical image at 1 mm/pixel resolution
				spectrometer	10 cm surface resolution, 620-1700 nm spectral range and spectral resolution of 10 nm	1 cm/pixel surface resolution, 350-1700 nm spectral range and spectral resolution of 6 nm	identify impact zone and subsurface spectral properties using before/after spec images	1+ spectral image at 1 cm/pixel resolution
		surface spectral distribution	linear surface resolution to a few decameters	spectrometer	spectral range of 620-2500 nm, spectral resolution of 10 nm	spectral range of 350-2500 nm, spectral resolution of 6 nm	execute imaging sequence within 8 months	spectral distribution of 2+ surface sites

Fig. 1 Science traceability matrix of the NEACO mission concept.

transfer until arrival at the sun-HO₃ L_1 point, at approximately 565 km from the asteroid, on April 1, 2027. The final approach is performed on the sunlit side of the asteroid, to allow for optical target acquisition. This arrival phase will also be used for final instrument checkouts and system checks before entering the science phases.

B. High-Altitude Hovering—45 km

The first science operations are performed during a hovering phase in which the pulsed plasma thrusters maintain a distance of approximately 45 km to the asteroid. In this phase, the narrow angle camera (NAC) maps the lit surface at 0.7 m/px, which is a resolution better than the required 1 m resolution for lit surface mapping.

The same optical images are used to generate the asteroid shape model at a resolution higher than the 5 m accuracy goal.

The 45 km altitude was selected for a number of reasons. First, it is a fairly safe distance for collision avoidance in the first phase of the mission where initial information about the asteroid is gathered. Second, it is well within the 50 km limit of the laser altimeter, which ensures that the altimeter can be used for both navigation and scientific information even if the spacecraft is drifting unexpectedly. Third, this altitude allows the NAC to capture images at resolutions better than the minimum requirement for lit surface mapping and shape modeling.

The asteroid's pole orientation will determine the visible and lit fraction of the asteroid surface, and will be extracted by applying

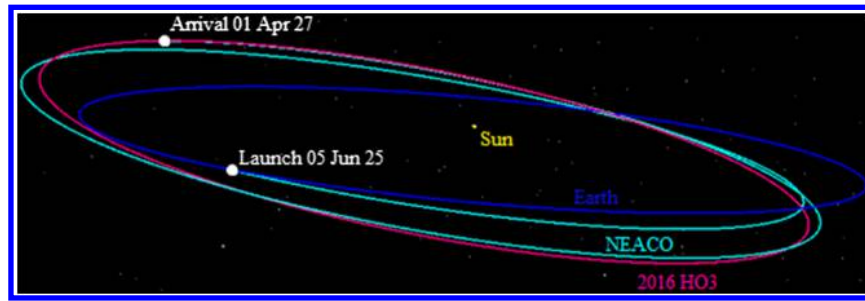


Fig. 2 Heliocentric orbit of the NEACO spacecraft.

landmark tracking to the NAC images using stereophotoclinometry. Landmark navigation was first demonstrated during the Near Earth Asteroid Rendezvous (NEAR) Shoemaker mission at asteroid 433 Eros [6]. It was used in combination with stereophotoclinometry during the ESA Rosetta mission about comet 67P/Churyumov-Gerasimenko [7], and will be used by NASA's OSIRIS-REx (Origins, Spectral Interpretation, Resource Identification, Security, Regolith Explorer) as well [8]. Once the pole orientation has been determined, the scheduling of the remaining imaging sequences can be modified to address the scientific goals. The duration of the high-altitude hovering phase is variable, and will be adjusted following examination of the asteroid's rotation pole and lighting conditions. The absolute maximum duration of this phase is 6 months, which occurs if HO₃'s rotation pole lies within its heliocentric orbit plane. In this case, the asteroid must be observed along half of its orbit for both poles to be seen in illuminated conditions. This is required because a full surface map is ideal for an accurate global shape model. However, in the event that such a pole orientation is found, the bulk of the surface images would be taken from the 45 km altitude, while any remaining images could be taken in the 10 km hovering phase.

C. Low-Altitude Hovering—10 km

After completion of the high-altitude hovering phase, the spacecraft descends to a lower altitude of 10 km. The resolution requirements of the surface spectroscopy are met by capturing spectral data at this altitude. The increased resolution of the NAC at this altitude also allows the shape model and surface map to be refined if necessary. At this altitude, both cameras are still able to view the entire asteroid, at a resolution of 15 cm/px for the NAC and 1 m/px for the medium-resolution backup camera. Although this phase provides higher-resolution imagery than the previous phase, and could conceivably replace most of the high-altitude hovering, the increased resolution comes at a cost of larger data files when similar compression is applied. Because of mission bandwidth limitations in communicating images back to Earth, this phase is not used for the bulk of optical surface imaging.

D. Mass Estimation Flybys

The spacecraft will perform a series of five low-altitude, hyperbolic flybys to estimate the asteroid's mass. The flyby trajectories, as described in Table 2, decrease in incoming hyperbolic velocity from 0.5 to 0.1 m/s and in periape radius from 2.0 to 0.6 km. The approaches are targeted to the B-plane formed by the sun-HO₃ and HO₃ orbital angular momentum vectors. The flyby sequences begin and end at a distance of 5 km from the asteroid, ranging in duration from 5 to 30 h. Including turnaround times of approximately 24 h,

the entire flyby phase lasts for roughly 10 days. Figure 3 summarizes the flyby sequence and hovering phases.

During each flyby, NEACO's laser altimeter provides a distance measurement to confirm the planned flyby geometry. The on-board cameras are also used on each flyby to observe HO₃'s surface. The closest flyby allows the NAC to capture images at a resolution of 1 mm/px, which is a resolution better than the 1 cm/px requirement needed to satisfy the high-resolution imaging goal. Using this flyby series, the 10% accuracy mass estimation goal is satisfied. Following completion of the flybys, the spacecraft returns to the 45 km hovering position while planning for the impactor operation is performed.

E. Strength Characterization

Before in situ observations by the Hayabusa and Rosetta missions, small bodies were thought to be free of regolith, due to the removal of loose particles from the surface by seismic shaking from (micro-) meteoroid impacts. However, these missions clearly showed the existence of regolith on the surfaces of asteroid Itokawa and comet 67P/C-G. These bodies are relatively large and have a slow spin period, such that the net (gravity + centrifugal) surface acceleration retains loose particles. Sánchez and Scheeres recently theorized that even small asteroids with fast rotation periods (the so-called "super-fast rotators") can retain regolith due to cohesive forces between small regolith particles, despite these bodies rotating faster than the critical spin limit [9]. Indeed, their theory and simulation suggest that regolith may exist on HO₃ at cohesive strengths as low as 0.02 Pa. Although it may exist as a global layer, it is most likely to be found in the polar regions of HO₃ at latitudes above 60 deg.

The final phase of the NEACO mission concept aims to validate the existence of regolith at the poles of HO₃ and to estimate the magnitude of surface cohesion, using a low-velocity impactor. The high-resolution surface images and spectroscopy obtained during low-altitude hovering will be examined to reveal the existence of regolith near the poles. More specifically, the visual reflectance and spectral reflectance of small regolith particles are distinctly different from that of the monolithic rock thought to form HO₃'s core [10]. A detailed mapping of the border between regolith-covered and regolith-free regions will help constrain the magnitude of cohesion between regolith particles and the monolithic (sub-)surface. Following this mapping, NEACO will descend toward one of the asteroid poles and hover at very low altitude. The spacecraft then releases a spherical probe using a spring mechanism and ascends again to a higher altitude while observing the probe impact. This impact, which occurs at the m/s level, will create seismic waves that are expected to remove regolith from certain regions on the asteroid surface, in particular near the impact site. By observing the regolith removal process and corresponding change in surface covering, NEACO will allow for an estimation of the magnitude of cohesion on asteroid HO₃ [9]. This strength characterization phase is illustrated in Fig. 4.

If regolith is, in fact, *not* found on the surface of HO₃, this will be a relevant observation that contrasts the predictions made by Sánchez and Scheeres about the super-fast rotator population. In this case, the impactor will be unable to provide much information about the (monolithic) asteroid surface. Because of the asteroid's fast spin period, it is not possible for the small impactor probe to settle on the

Table 2 Mass estimation flybys

Flyby No.	V_{∞} , m/s	b_p , km	t , h	ν_i, ν_f , deg	$3\sigma_H$, %
1	0.5	2.0	5.56	68.2	260.2
2	0.4	1.5	6.94	73.3	82.9
3	0.3	1.0	9.25	78.7	17.6
4	0.2	0.8	13.86	80.9	4.6
5	0.1	0.6	27.32	83.2	0.6

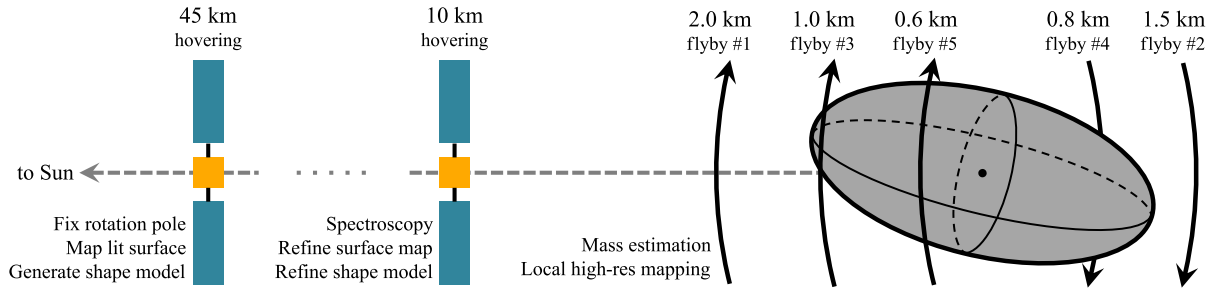


Fig. 3 Illustration of the mission concept.

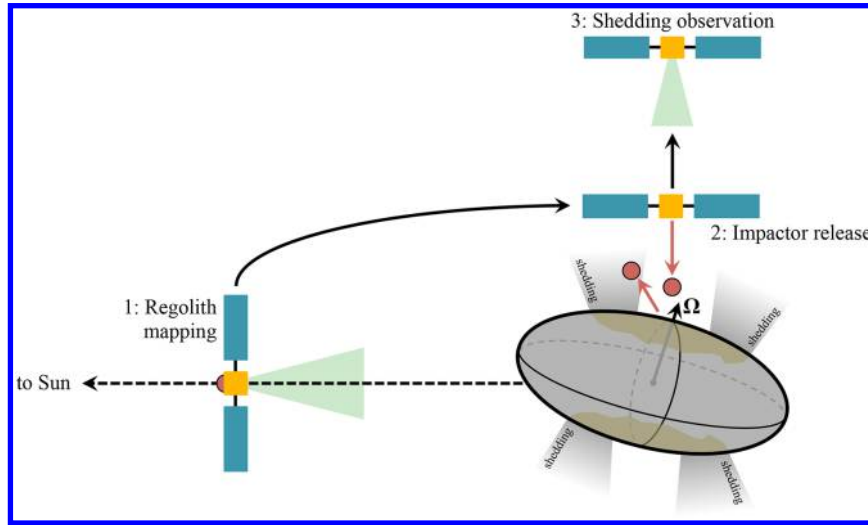


Fig. 4 Illustration of the strength characterization phase.

surface. Nevertheless, the impactor will be deployed and its impact observed, as the velocity changes that occur over the impact may provide information on the structure and dissipative properties of the surface, through an estimation of the coefficient of restitution [11].

IV. Spacecraft Design

A. Instruments

1. Optical Imaging Suite

The optical imaging suite includes a high-resolution NAC, and a backup medium-resolution camera (AMICA) for redundancy. Figure 5 plots the altitudes at which the different cameras can satisfy

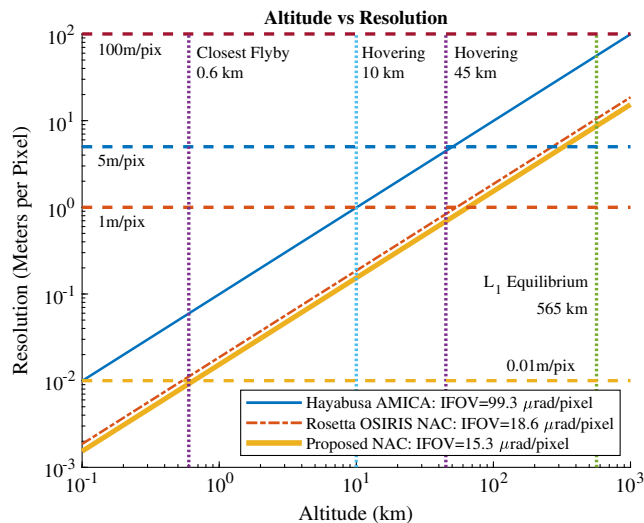


Fig. 5 Optical camera resolution at various altitudes.

the various resolution requirements, and Table 3 gives relevant camera specifications. The proposed NAC has a narrow overall field of view and a narrow instantaneous field of view (IFOV) that enables high-resolution imaging at higher and safer altitudes than the AMICA. The Rosetta OSIRIS NAC is used as an upper bound reference for mass and volume estimation for the proposed NAC, as well as a reference for other NAC specifications. The Rosetta NAC has strict requirements on performance such as stray light rejection for gas and dust imaging [12] that require an optical path with larger footprint than is necessary for NEACO. Thus, the proposed NAC, with a similar IFOV, allows for a similar design with reduced volume and mass requirements. Note that in Table 3, a smaller charge-coupled device (CCD) pixel size can be selected for the proposed NAC to allow for a smaller focal length to meet the required IFOV. Alternative options that may meet the mission requirements include a CubeSat form factor Ritchey-Chrétien telescope [13] or a space-qualified version of a ground telescope with the desired focal length [14].

The proposed medium-resolution camera is based on the Asteroid Multi-Band Imaging Camera (AMICA) instrument flown on the Hayabusa-1 mission [15]. In the event of NAC failure, all science goals will still be achievable. The high-altitude (45 km) hovering phase would be eliminated, with global lit surface mapping instead occurring at the 10 km altitude hovering position with the AMICA. This will allow NEACO to generate a full surface map at the desired resolution of 1 m/px. Although the AMICA can image the asteroid at a 5 m/px resolution at the high-altitude hovering position for shape model reconstruction, redundant images at a higher resolution would still be required at the lower altitude in order to generate the global lit surface map. A close terminator orbit or close hovering would also be required in order to satisfy the 1 cm/px high-resolution mapping requirement. The AMICA camera also allows NEACO to use optical images for center-finding-based navigation down to altitudes of 500 m, whereas the NAC can do center-finding only down to a roughly 3 km altitude.

Table 3 Camera specifications

	AMICA	Proposed NAC	Rosetta NAC [12]
IFOV, $\mu\text{rad}/\text{px}$	99.3	15.3	18.6
Field of view, deg	5.83×5.69	0.9×0.9	2.2×2.2
CCD format, px	1024×1000	1024×1024	2048×2048
CCD pixel size, μm	12	12	13.5
Focal length, mm	120	784	717
Aperture, mm	15	75	87.5

Table 4 Spectrometer specifications

	Argus	Modified SWIS
Spectral range, nm	1000–2500	350–1700
Spectral resolution, nm	6	5.7
Field of view, deg	0.15×0.15	0.29
	(point)	(slit)
Spatial elements	1	300

Table 5 Propulsion specifications

	8 cm XiPS	μCAT
Thrust	2–14 mN	1–50 μN
I_{sp} , s	2000–3000	2500–3000
Total efficiency, %	55.0	15
Mass, kg	2.0	0.2
Total input power, W	100–350	2–14

Space 1 and Dawn spacecraft [20]. Two thruster units will be able to provide the long required thrusting time, as the life-limiting components were tested in the 13 cm XiPS through more than 21,000 h of operation [21]. NEACO is also equipped with six Micro-Cathode Arc Thrusters (μCAT s) to allow for both hovering and reaction wheel desaturation operations. The μCAT has been flight-tested and has a TRL of 7/8 [22]. The pulsed plasma thrusters can also be used for attitude maneuvers and reaction wheel desaturation [23]. Table 5 lists the expected specifications for the 8 cm XiPS and the μCAT .

2. Power

The power system is primarily designed toward the requirement of providing sufficient power to the electric propulsion system (EPS) during the cruise phase. Hence, the solar panels are sized to allow for continuous nominal EPS operation, without relying on batteries. At a distance from the sun of 1 AU, they produce approximately 396 W of power. This power level is more than enough to power both the SEP and communications/instruments in the low-thrust trajectory phase. In the event of attitude deviations, a secondary battery allows for 2.5 h of continuous thruster use before the spacecraft enters a safe mode or phoenix mode (only spacecraft computer and radio receiver running).

3. Attitude Determination and Control

The NEACO attitude determination and control system (ADCS) package is based on Blue Canyon Technologies' Microsat Spacecraft sensor bundle [24] and FlexCore control system [25]. This package provides a 1σ 0.002 deg 3-axis pointing accuracy in addition to a 1 arcsec/s pointing stability over 1 s. These accuracy specifications ensure sufficient stability to provide the required image quality.

4. Communications and Data Handling

The NEACO spacecraft is equipped with four patch antennas to receive communications from Earth, placed on different panels to enable full-sky coverage. The antennas have a gain of 9–11 dB and are able to transmit low-bandwidth telemetry data, such that two-way housekeeping communication is possible at all times, without requiring specific spacecraft attitudes. The spacecraft is equipped with an X-band transmitter for high-bandwidth communications, that is, the transmission of instrument measurements. Reflect array panels are placed on the backside of the solar arrays to boost the X-band gain to 23 dB. This placement avoids the inclusion of communication-only deployables and reduces the mass and volume of the communications and data handling (C&DH) subsystem. As the resulting X-band transmission system has a beam width of approximately 10 deg, the spacecraft will usually need to rotate into an Earth-pointing attitude in order to transmit high-bandwidth data. In other words, instrument measurements and data transmission are unlikely to occur at the same time. This does allow the spacecraft to dedicate high power levels to the X-band system when in use. Note that on-board batteries allow for 2 h of transmission at maximum power. The solar arrays will further extend this time in most geometries.

Although the link budget will vary based on the power available to the spacecraft, the worst-case scenario (i.e., lowest power available) can be computed to give an idea of how the link budget will impact mission operations. The point at which the least amount of power is available to the spacecraft occurs when it is at its farthest distance from the sun. This occurs 25 days after arrival at HO_3 , with an output of no more than 325 W. This corresponds to an Earth/ HO_3 distance of 0.19 AU. From the total 325 W provided by the solar arrays, a maximum of 125 W is dedicated to the radio frequency (RF) chain,

2. Spectrometers

Two separate spectrometers have been included in this mission in order to gather a wide range of surface spectral information. Table 4 gives the necessary specifications for the two NEACO spectrometers. The Argus 1000 IR Spectrometer is a commercial off-the-shelf (COTS) solution for coarse spectroscopy that provides spectral information at larger wavelengths from a single spatial area. At the 10 km hovering altitude, the Argus spectrometer covers a 26×26 m spatial footprint on HO_3 , giving very coarse information on surface spectral properties at wavelengths from 1000 to 2500 nm. The Snow and Water Imaging Spectrometer (SWIS) instrument [16] is used as a baseline design for a spectrometer that covers lower wavelengths (350–1700 nm), while also having more spatial resolution than the Argus spectrometer. Unlike the Argus, the SWIS instrument simultaneously collects spectral data from points along a one-dimensional line (i.e., a “slit” instead of a “point” source spatially). Because the SWIS is designed with a wide field of view to accommodate Earth observation, the baseline design uses a modified SWIS instrument with optics that provide a narrower field of view that fully covers HO_3 's 50 m diameter at an altitude of 10 km. Further, the SWIS instrument has 600 spatial elements, which would be far too many for HO_3 , and so the modified SWIS has only 300 spatial elements. This gives a spatial resolution of about 17 cm at an altitude of 10 km. As more information is gathered during science operations, regions of particular interest, including the impact site, can be further investigated using these instruments and lower altitude hovering or flybys.

3. Altimeter

To improve the shape model scaling, gravity estimation flybys, optical navigation, and overall spacecraft safety, NEACO is equipped with a laser altimeter. The reference design for the NEACO altimeter is the laser-altimeter flown on board Hayabusa-1 [17], which has a range from 50 m to upward of 50 km [18]. This operational range allows the spacecraft to use the altimeter during all science phases of the mission. The altimeter has a mass of 3.56 kg and a power consumption of 22 W [18].

B. Spacecraft Bus

1. Propulsion

Preliminary trade studies identified the 8-cm-diam Xenon Ion Propulsion System (XiPS) [19] as a viable SEP system for the considered class of small spacecraft. The 8 cm XiPS system follows a long series of flight-proven hardware. Since 1997, the larger 13 cm XiPS has been used for Boeing satellite station keeping; dozens of next-generation 25 cm XiPS have also flown [20,21]. The new 8 cm XiPS incorporates improvements from both the 25 cm XiPS and 30 cm NSTAR. The latter is known for its success on NASA's Deep

leaving 200 W available for the rest of the spacecraft subsystems; 25 W of RF power is thus effectively transmitted to the transmitting channel, assuming 20% of power conversion efficiency. With a 150 bit/s bitrate, the link margin amounts to 3.57 dB.

This data rate is then used to estimate how long it will take to transmit an image back to Earth. At an altitude of 45 km, the NAC resolution is 0.692 m/px, which results in HO₃ being enclosed within a square of roughly 35 × 35 pixels. This figure is rounded up to 50 × 50 pixels, and assuming that all other pixels can be cropped out, there is a total of 2500 pixels of information to store and/or transmit. Further assuming that each pixel is encoded over 12 bits without compression, the center pixels would require 30,000 bits of storage space, which can be transmitted back to Earth in 200 s, assuming a constant 150 bit/s bitrate. The applied power can be increased to allow for faster data transmission, or decreased to leave more power available to the spacecraft subsystems. Data compression will also be applied to reduce the 12 bits/pixel figure, which will decrease the amount of transmission time necessary. The budget makes use of the Deep Space Network (DSN) as a baseline, but can also use smaller ground stations such as Atlas to reduce operational costs.

5. Mass and Volume

The spacecraft bus is designed to provide radiation shielding and sufficient surface area to stow the solar arrays, with dimension 50 × 50 × 70 cm. Significant margin is allocated for low-TRL components; high-TRL components are given a smaller margin. The internal volume available for system design and instrumentation is reduced to 40 × 40 × 60 cm after accounting for structural elements and solar arrays. All of the proposed asteroid facing instruments, that is, the NAC (estimated maximum size corresponding the Rosetta NAC), AMICA, spectrometers, and altimeter, can fit on the 40 × 40 cm face with room to spare for thrusters. A summary of the mass budget with rounded values is provided in Table 6. Although aggregate contingency percentages are shown here by category, actual contingency percentages are selected and applied to each individual component based on its flight readiness. There is also an additional 25% margin added to the total spacecraft mass that includes individual

component contingencies. Thus, the final mass of 165.5 kg is a highly conservative estimate of the total wet mass at launch.

6. Thermal

NEACO's thermal subsystem maintains the spacecraft temperature within the allowable operating range during nominal operations. The subsystem is cold-biased, as the solar arrays provide sufficient heat when deployed. To achieve this cold-biasing, reflective coating and tapes are applied to the exterior bus. The applied silver Teflon tape has proven flight heritage from the MinXSS and QB-50 Challenger cubesats, and offers excellent thermal insulation.

V. Key Mission Analyses

A. Trajectory

The NEACO trajectory was designed to conform to the Vega launch specification of $C_3 \leq 25 \text{ km}^2/\text{s}^2$ possible for a wet mass up to 180 kg. Launch from Guiana Space Center constrains the departure declination to $\pm 5.2^\circ$. Preliminary trajectory design considered launch opportunities as a secondary payload with the constraint $C_3 \leq 0$ and a maximum wet mass of 140 kg [4]. The first step in the trajectory design process weighed high-thrust versus low-thrust propulsion and the use of gravity assists. The $C_3 \leq 0$ constraint, combined with HO₃'s relatively large inclination of 7.77° , limits the use of classic, chemical propulsion. The smallest ΔV transfer identified required a total ΔV of 4.8 km/s and spanned 269 days. For a wet mass of 140 kg, this only allows between 12 and 42 kg of delivered mass for I_{sp} values between 200 and 400 s. The latter value would be difficult to provide, as 4.4 km/s would be needed for rendezvous at the end of the transfer. Cryogenic boil-off would reduce the achievable I_{sp} on this mission.

A chemical mission using lunar flybys was considered, but rapidly discarded. Besides imposing high navigation accuracy requirements a few days postlaunch, they can be performed only twice per month. Furthermore, the spacecraft would need a relative velocity to the moon of approximately 4.3 km/s. At this high relative velocity, the moon provides only a small turning angle; that is, the lunar flyby would not provide sufficient inclination change. A chemical mission using combinations of Earth and/or Venus flybys was also discarded, due to excessive propellant requirements and/or times of flight.

Solar electric propulsion was selected as the choice low-thrust propulsion option. Solar sailing was initially investigated, but was ruled out due to challenges in dealing with solar radiation pressure (SRP) near HO₃. To that end, maximum payload trajectories were computed using the Evolutionary Mission Trajectory Generator (EMTG) [26] to complete the propulsion system trade study, identify launch and arrival windows, and determine the effectiveness of an Earth gravity assist. Having neglected the use of a lunar flyby, choosing to use the maximum allowable $C_3 = 0$ for the preliminary trajectory ensured that time and fuel were not wasted to depart Earth. The preliminary trajectory design effort resulted in a 2-year, low-thrust, and Earth flyby trajectory that remains a viable option if a dedicated launch proves elusive.

The dedicated launch adds sufficient energy to remove the complexity of a gravity assist, improve the delivered mass, and reduce the flight time. A grid of low-fidelity solutions, subject to two-body dynamics en route to HO₃, was produced beginning with Earth's heliocentric position and velocity plus launch ΔV . Low-thrust propulsion was modeled by impulsive maneuvers separated by Keplerian arcs. Rendezvous with HO₃ facilitates extended science operations at the asteroid, as opposed to a flyby trajectory. Thrust and specific impulse were fixed to 9 mN and 2500 s, respectively, which correspond to 223 W input power to the 8 cm XiPS thruster. A 90% duty cycle was assumed. These are conservative thruster specifications so that significant improvements to the trajectory will be possible if the full 8 cm XiPS performance range in Table 5 is attainable.

Direct transfer options, that is, those without gravity assists, are detailed in Fig. 6. Contour lines of wet mass are superimposed on the delivered mass to point out that maximum payload trajectories do not necessarily use the maximum allowable wet mass. Favorable transfer opportunities repeat approximately every 6 months.

Table 6 Mass budget

Subsystem	Mass, kg	Contingency, %	Total mass, kg
Structure	32.0	10	35.2
Antennas	3.5	15	4.0
Bus components total	55.6	7	60.0
XIPS thrusters (2)	4.0	5	4.2
XIPS thruster power processing unit	7.0	5	7.4
Fuel mass	20.6	10	22.7
Pulsed plasma thrusters (6)	1.2	10	1.3
Solar array	6.0	10	6.6
Blue Canyon XB MicroSat	7.5	5	7.9
System			
X-band radio board	0.4	15	0.5
Reaction wheels (3)	4.8	5	5.0
Tri-directional sun sensors (6)	0.1	15	0.1
2 cell battery packs (30)	3.0	5	3.2
Fuel tank	1.0	20	1.3
Fasteners	1.0	15	1.2
Harness	2.0	15	2.3
Staking/coating	1.0	15	1.2
Payloads total	23.9	20	28.7
Argus spectrometer	0.2	10	0.3
AMICA camera	5.7	10	6.3
Altimeter	3.6	10	3.9
Impactor system	1.5	35	2.0
Narrow-angle camera	11	25	13.8
Modified SWIS	1.8	31.5	2.4
Subtotal			132.4
Total	132.4	25	165.5

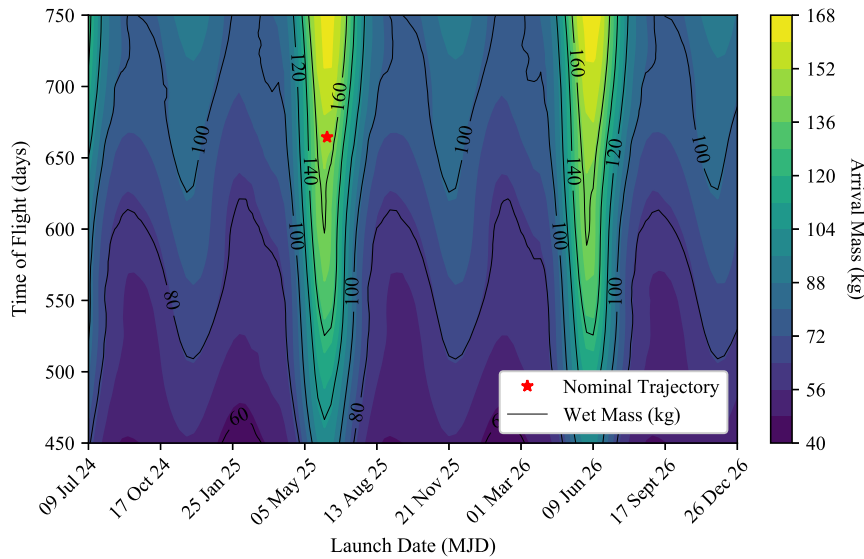


Fig. 6 Maximum payload delivered to HO₃ with direct transfer.

A nominal trajectory was selected from the grid for further optimization. The point was selected to minimize the time of flight for the known spacecraft arrival mass for the NEACO design. While the nominal trajectory was chosen from an earlier family in Fig. 6 because it had a slightly lower time of flight, trajectories with later launch dates are also viable due to the repeating instances of favorable launches. The next iteration after the grid solution improved the model fidelity and produced a fully integrated, continuous trajectory. The impulsive maneuver approximation was replaced with finite-burn low-thrust, and third-body perturbations from the Earth, moon, Mars, and Jupiter were included in the heliocentric propagation. The resulting trajectory can be seen in Fig. 2. This transfer takes 665 days to deliver 144.9 kg from an initial mass of 165.5 kg. Given that 396 W is available from the solar panels at 1 AU, increased solar distance in the final trajectory never causes the power available to fall below 300 W. This gives plenty of power margin for the thrusters throughout the trajectory.

B. Visual Acquisition

An important operational consideration for the mission is visual acquisition of the asteroid early enough to adjust the trajectory to account for the true asteroid position. Although the uncertainty on the JPL Horizons ephemeris does not exceed 100 km during the interplanetary phase, it is still important to refine the trajectory as early as possible to prevent the need for drastic trajectory correction maneuvers. A signal-to-noise ratio (SNR) of 5 is used as a threshold for estimating the earliest time at which the asteroid can be visually acquired using a given camera. The first step in estimating SNR is calculating the apparent magnitude of HO₃ along the spacecraft's trajectory, based on the absolute magnitude of 24.3. Muinonen et al. give expressions for estimating the apparent magnitude of an asteroid [27], the most important of which is the apparent magnitude expression in Eq. (1).

$$m_v = H(\chi) + 5 \log_{10} R R_{\odot,b} \quad (1)$$

Here, χ is the angle between the HO₃-sun and HO₃-spacecraft lines and assumed to be $\geq 7.5^\circ$, R and $R_{\odot,b}$ are the relative distance between the spacecraft and HO₃ and the sun and HO₃ in AU, the slope parameter G is taken to be 0.15 (see Ref. [27]), and m_v is the apparent visual magnitude. The relation between apparent magnitude and flux, which is used to calculate the number of photons incident on the CCD, is given in Eq. (2), where F is the flux of HO₃ and F_0 is the reference flux for the visual band ($F_0 = 3640$ Jy).

$$F = F_0 \times 10^{-0.4m_v} \quad (2)$$

Given that J_y is equal to 1.51×10^{-7} photons/s/m²/($\Delta\lambda/\lambda$), and for visible wavelengths $\Delta\lambda/\lambda = 0.16$, the number of visible band photons collected per second by a telescope with aperture $A = \pi\phi^2/4$ is

$$f = F \times 1.51 \times 10^7 \times \left(0.16 \frac{\pi}{4} \phi^2\right) = 1.897521 \times 10^6 \times (F\phi^2) \quad (3)$$

where F is the flux measured in Jy and ϕ is the diameter of the telescope in meters. However, not all of these photons reach the CCD sensor due to optical considerations such as a secondary mirror shadowing the primary mirror ($\sim 10\%$), losses at each mirror reflection ($\sim 10\%$), and optical transmission losses ($\sim 30\%$). The CCD sensor also has a quantum efficiency, which gives the fraction of incident photons that are actually detected by the sensor. For this analysis a quantum efficiency of 50% over all wavelengths is assumed in order to avoid integration. This results in an effective photon rate of $f^* = \zeta f = (0.9)^2 \times 0.7 \times 0.5 f \simeq 0.28 f$.

To assess whether or not HO₃ is detectable, this photon rate must be compared with the background photons detected and sensor noise using the SNR given by [28]:

$$S/N = \frac{f^* t_e}{\sqrt{f^* t_e + f_{\text{sky}}^* t_e + D t_e + N_r^2}} \quad (4)$$

The night sky brightness is estimated to be $\bar{m}_{\text{sky}} = 22$ mag/arcsec² [29]. Hence, the number of sky photons collected by a camera per second and per arcsecond square is

$$\bar{f}_{\text{sky}} = \bar{F}_{\text{sky}} \times 1.51 \times 10^7 \times \left(0.16 \frac{\pi}{4} \phi^2\right) = 1.897521 \times 10^6 \times (F_{\text{sky}} \phi^2) \quad (5)$$

with $\bar{F}_{\text{sky}} = 5.7690 \times 10^{-6}$ Jy/arcsec². The dark current D and read noise N_r are estimated using values provided by the Hayabusa AMICA [15] and Rosetta OSIRIS [12] reports when calculating SNR for the AMICA and proposed NAC, respectively. Calculating SNR for the NEACO trajectory using Eq. (4) shows that the AMICA can acquire the asteroid roughly 24 days before arrival, noting that it has a maximum exposure time of 178 s. The proposed NAC can acquire HO₃ at roughly 1.5 months before arrival. Acquisition at 1.5 months gives plenty of time to adjust the trajectory, whereas acquisition at 24 days is a reasonable amount of time given that the uncertainty in

HO₃'s position is relatively low. The proposed NAC aperture of 75 mm could be reduced in order to save volume, which would move the acquisition time closer to arrival. However, the larger aperture allows for faster exposure times during the science orbits, which reduces the ADCS requirements to achieve sharp images. Alternatively, the NAC aperture could be increased in order to support an earlier visual acquisition of HO₃.

C. Relative Dynamics

The system equilibrium points, hovering altitudes, and allowable mission operation phases are determined by using a three-body dynamics analysis. This analysis is crucial in dictating the allowable science phases for the mission.

1. Equations of Motion

The equations of motion for a mass particle subject to the gravitational attraction of HO₃, solar gravity, and radiation pressure are derived as in Scheeres and Marzari [30]. The potential function is:

$$\mathcal{V}(\mathbf{r}) = \mathcal{U}(\mathbf{r}) + \frac{\mu_{\odot} - \beta}{\|\mathbf{r}_{b\odot} + \mathbf{r}\|} + \frac{\mu_{\odot} + \mu}{r_{b\odot}^2} \hat{\mathbf{r}}_{b\odot} \cdot \mathbf{r} + \mathbf{u} \cdot \mathbf{r} \quad (6)$$

where $\mathcal{U}(\mathbf{r})$ is the gravitational potential of HO₃, μ is the gravitational parameter of the sun, $\beta = C_r(\Phi_{\odot}/c)AU^2/B$ is the SRP parameter, $\mathbf{r}_{b\odot}$ is the position vector of HO₃ with respect to the sun, \mathbf{r} is the relative position vector of the spacecraft as seen from HO₃, and \mathbf{u} is the input vector (i.e., the applied thrust). Furthermore, $\Phi_{\odot} = 1367 \text{ W/m}^2$ is the solar irradiance, c is the speed of light, AU is the astronomical unit in meters, $C_r \approx 1.3$ is the coefficient of reflectivity, and B is the mass-to-cross-sectional-area ratio of the spacecraft.

For this analysis the equations of motion in a pulsating synodic reference frame \mathcal{S}' centered at HO₃'s center of mass and rotating about the sun with HO₃ have been derived. For brevity, the final form of the equations is shown without derivation in Eq. (7):

$$\begin{cases} x'' - 2y' = \frac{1}{1+e\cos\nu} (\tilde{g}_x + \tilde{\beta} + 3x + \tilde{u}_x), \\ y'' + 2x' = \frac{1}{1+e\cos\nu} (\tilde{g}_y + \tilde{u}_y), \\ z'' + z = \frac{1}{1+e\cos\nu} (\tilde{g}_z + \tilde{u}_z) \end{cases} \quad (7)$$

in which:

$$\tilde{\mathbf{r}} = \frac{\mathbf{r}}{er_{b\odot}} \quad \text{and} \quad \tilde{\mathbf{v}} = \frac{1}{r_{b\odot}} \left(\frac{\mathbf{v}}{e\dot{\nu}} - \tilde{\mathbf{r}} r'_{b\odot} \right) \quad (8)$$

are the normalized position and velocity coordinates of the spacecraft in the \mathcal{S}' frame, and

$$\tilde{\mathbf{g}} = \frac{e^2 r_{b\odot}^2}{\mu} \mathbf{g} \quad \text{with} \quad \varepsilon = \sqrt[3]{\frac{\mu}{\mu_{\odot}}} \quad (9)$$

is the normalized gravitational acceleration of the asteroid. In this expression, ν is the true anomaly of asteroid HO₃, and the heliocentric distance $r_{b\odot}$ of HO₃ is defined as

$$r'_{b\odot} = \frac{r_{b\odot}^2 e \sin \nu}{a(1-e^2)} \quad \text{with} \quad r_{b\odot} = \frac{a(1-e^2)}{1+e\cos\nu} \quad (10)$$

2. Equilibrium Points and Periodic Orbits

A first step toward understanding the system dynamics is ignoring HO₃'s eccentricity and determining the natural equilibrium points \mathbf{x}^* . Two solutions are found using this assumption, namely, $x_{L_1} < 0$ and $x_{L_2} > 0$. The exact location on the x axis depends on the value of the normalized SRP parameter $\tilde{\beta}$. The second equilibrium point necessarily lies opposite of the sun and in the shadow of HO₃. This location is not affected by SRP, but also would not allow for solar power to be collected with solar panels. For this reason, its use is not

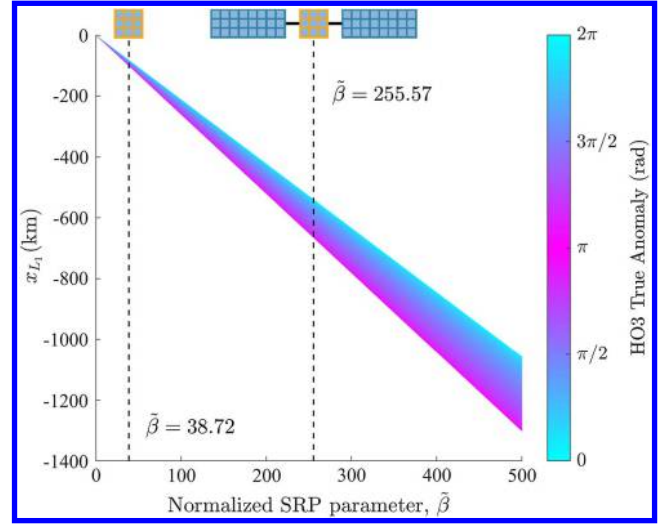


Fig. 7 L_1 periodic orbit for different $\tilde{\beta}$ values.

considered for proximity operations, and the L_1 point alone is further investigated with the inclusion of HO₃'s eccentricity.

When $e \neq 0$, the L_1 equilibrium point becomes a periodic orbit where the spacecraft moves back and forth along the sun-HO₃ line. The size of the periodic orbit depends on the mass-to-area ratio of the satellite and can be inferred from Fig. 7, which shows the evolution of the same periodic orbit for a range of $\tilde{\beta}$ values.

When NEACO's solar arrays are fully deployed and facing the sun, the cross-sectional area of the spacecraft is roughly 1.65 m^2 . Knowing that the delivered mass of the spacecraft is approximately $m = 140 \text{ kg}$, the nominal value of the normalized SRP parameter is $\tilde{\beta} = 255.57$. This configuration allows for a periodic orbit with x coordinates between -511 km and -630 km (567 km mean), as measured from the center of the asteroid. This periodic orbit is mildly unstable with unstable eigenvalue $\lambda_u = 1.0142$. This small instability makes the L_1 periodic orbit particularly attractive for parking the spacecraft upon arrival and performing several subsystems checks before moving into science orbits at lower altitudes.

3. Spacecraft Hovering

Figure 7 demonstrates that orbiting in an L_1 periodic orbit at a distance feasible for asteroid surface mapping is not possible, even when the solar panels of NEACO are either folded or perpendicularly tilted ($\tilde{\beta} = 38.72$; periodic orbit ranging from -79.85 km to -98.42 km). Accordingly, there are no natural orbits that keep the spacecraft altitude fixed at the desired values. Instead, the team opted for a hovering approach and assessed the amount of ΔV required for each of the hovering phases proposed in the mission profile.

Let $\mathbf{x}^* = [x^* \ 0 \ 0 \ 0 \ 0 \ 0]^T$ be the desired state of the satellite in the \mathcal{S}' frame, where x^* is either 45 or 10 km. From Eq. (7), it can be readily seen that $\tilde{u}_y = \tilde{u}_z = 0$, whereas

$$\tilde{u}_x = -\tilde{\beta} - \tilde{g}_{x^*} - 3x^* \quad (11)$$

Figure 8 displays the acceleration profiles required to counteract the effect of gravity and solar radiation pressure at different orbital regimes over 1 year. Per month, 0.1762 and 0.1637 m/s are required for hovering at 10 and 45 km, respectively. Although the difference between these two cases is on the order of a few mm/s/month, the values provide only an estimate of the ΔV necessary for hovering. Several factors must be included for the actual mission design. First, the thrusters of NEACO shall be stopped during the scientific operations and communications of the spacecraft. However, because both of the hovering positions are unstable with eigenvalues 1.755 and 134.9, respectively, more maneuvers are needed in order to return the spacecraft back to its nominal position. Second, navigation errors and mis modeled dynamics shall be included in the initial state and orbital propagation of the satellite. Deviations from the nominal initial conditions would grow exponentially along the unstable

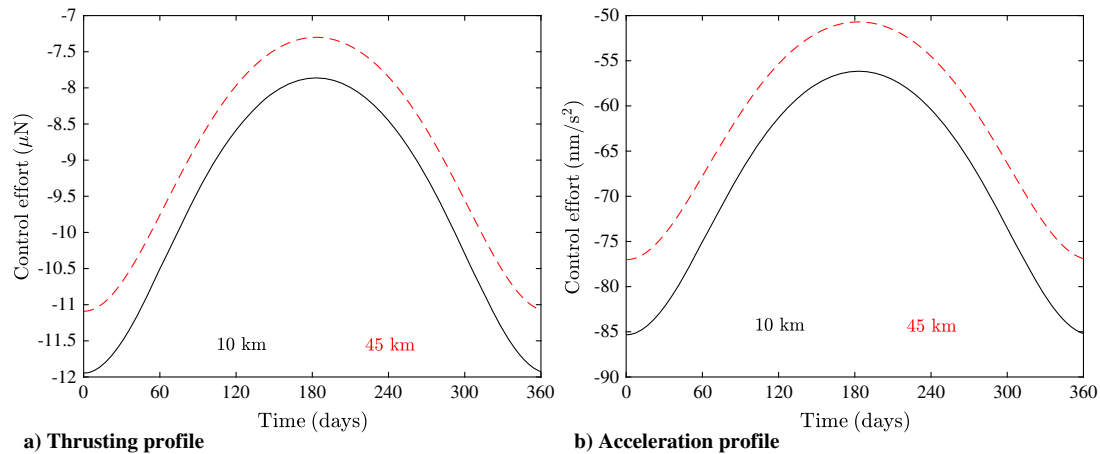


Fig. 8 a) Thrusting and b) acceleration profiles for different hovering altitudes.

manifold of the hovering point, and additional control effort is mandatory in order to nullify undesired growths. A conservative estimate of total ΔV needed to complete all hovering phases, including these additional factors not accounted for in the 0.1762 m/s/month and 0.1637 m/s/month figures, is 1.5 to 2 m/s. This range of total ΔV and thrust levels can be easily handled by the pulsed plasma thruster system on board NEACO.

4. Terminator Orbits

Terminator orbits typically allow for stable spacecraft operations close to the asteroid surface, where the dynamics are strongly perturbed by the irregular gravity field and solar radiation pressure. In such an environment, terminator orbits are frozen and approximately circular, allowing for consistent resolution coverage of the asteroid surface [31]. Furthermore, such orbits remain clear of the asteroid shadow and thus provide constant maximum power availability to the solar arrays. However, for these orbits to be possible, the area of spacecraft with respect to the sun must be relatively low. On the one hand, if the spacecraft area-to-mass ratio is high, terminator orbits may be too close to the surface of HO₃ to be safely operated. On the other hand, a properly designed terminator orbit naturally precesses with respect to the sun and may survive for a long time, in spite of the highly perturbed dynamical environment of an asteroid [31]. Further optimization is possible by exploiting the attitude-orbit coupling resulting from strong solar radiation pressure effects [32].

To investigate the applicability of terminator orbits to the NEACO mission concept, a Monte Carlo analysis is performed. In this analysis, orbit simulations are performed with uncertainties on the asteroid mass, SRP parameter β , and the initial spacecraft state shown in Table 7. Table 8 provides results on the most critical terminator orbit, that is, the orbit with semimajor axis $a = 150$ m that is necessary in the event of a NAC failure, when such a low altitude is necessary for the AMICA camera to satisfy the high-resolution imaging requirements. The table includes the shortest failure time (SFT), average failure time (AFT), and longest failure time (LFT). These results show that this orbit carries a small chance (0.10%) of impacting with the asteroid within 4.67 days from insertion and a 26.00% probability of escaping from the system within similar time

scales. Simulations for orbits with semimajor axes of 100 and 200 m were also run, with the safest orbit in terms of impact probability appearing to be the 200 m case (zero chance of impact).

While the Monte Carlo analysis here has shown a low chance of impacting the asteroid, using terminator orbits for nominal mission operations has not been proposed in the baseline mission for a number of reasons. First, a great deal of analysis with more certainty in asteroid parameters must be performed in order to validate the safety of an orbit that lies so close to the asteroid surface. For example, if the asteroid is assumed to have an ellipsoidal shape, the impact probabilities are much greater [4]. Many of the asteroid parameters that are needed for more accurate terminator orbit analysis must be found in the main science phase, and so terminator orbits are not ideal to use for surface mapping. Further, as shown in the previous section, using a hovering approach for main science operations requires very low levels of ΔV with very low mass thrusters. Thus, the mission is not adversely affected by using an active control approach as opposed to attempting to enter a natural terminator orbit about HO₃.

D. Gravity Estimation

The flybys described in the mission concept are designed to estimate the mass of HO₃ by observing the passage time between two mirroring true anomaly angles in a hyperbolic trajectory. This method, developed by Takahashi and Scheeres [33] and denoted as the μ_{\parallel} parameter estimation method, observes the difference between the expected passage time when no asteroid gravity is present and the actual time of passage when passing under the influence of HO₃'s gravity. The very small mass assumed for HO₃, with a sphere of influence at $r_{SOI} = 0.235$ km, requires these close flybys in which the effect of the asteroid's gravity can be observed and measured.

Table 2 presents the five flybys trajectory parameters and expected performances. The parameters are the incoming hyperbolic velocity V_{∞} , the expected radius of periape b_p , the expected passage time t (under the influence of HO₃'s gravity), the incoming and outgoing true anomaly angles ν_i and ν_f (set to be equal), and the expected 3-sigma error in HO₃ gravitational parameter estimation σ_{μ} . For all flybys, the passage is defined between 5 km before and after the B-plane crossing. For this sequence of flybys, the final $3\sigma_{\mu}$ value of 0.6% with $\mu = 0.013$ m³/s² increases only to 0.85% when taking $\mu = 0.009$ m³/s². Thus, the asteroid density variation considered in

Table 7 Monte Carlo input errors

Error source	Variable	Uncertainties
HO ₃ initial true anomaly	ν_0	$\nu_0 = \mathcal{U}([0, 2\pi])$
HO ₃ gravitational parameter	μ	$3\sigma_{\mu} = 0.10\mu$
S/C SRP parameter	β	$3\sigma_{\beta} = 0.10\beta$
S/C initial position error	\mathbf{r}_0	$1\sigma_{r_0} = 1$ m
S/C initial velocity error	\mathbf{v}_0	$1\sigma_{v_0} = 1$ mm/s

$\mathcal{U}_x([a, b])$ denotes a uniform distribution for the continuous random variable $x \in [a, b]$.

Table 8 Monte Carlo simulation for terminator orbit with 150 m semimajor axis

	Chance, %	SFT [d]	AFT [d]	LFT [d]
Impact	0.10	4.67	4.67	4.67
Escape	26.00	3.38	5.25	33.92
Success	73.90	—	—	—

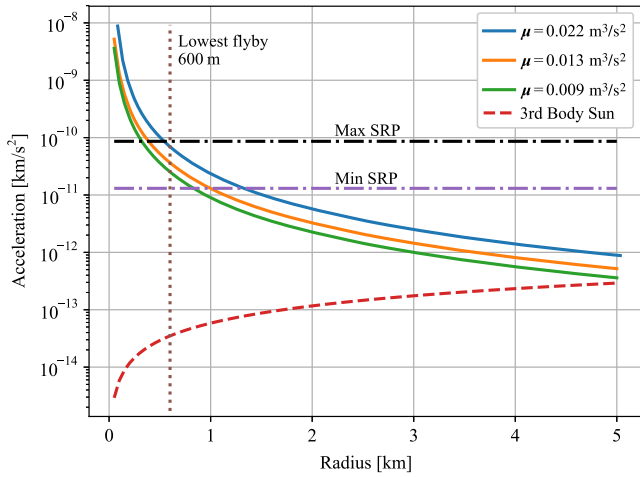


Fig. 9 Acceleration magnitudes in the HO_3 environment.

this study is not expected to significantly impact the gravity estimation analysis.

Note in Table 2 that the expected gravitational parameter estimation error after the fifth and final flyby is substantially smaller than the targeted 10% error. This added tenfold factor is put in place to account for the lack of SRP consideration in the $\mu_{||}$ method. Figure 9 shows the dominant accelerations felt by the spacecraft near HO_3 in the HO_3 frame. These accelerations include the gravitational pull of HO_3 , for the nominal asteroid density as well as the higher and lower density cases, as well as the minimum and maximum SRP accelerations and the sun's third body perturbation. The figure shows how the gravitational acceleration decreases compared with the fixed SRP acceleration for both the maximum and minimum SRP configurations. At the minimum distance flyby ($b_p = 0.6$ km) the maximum SRP acceleration is in the same order of magnitude as HO_3 's gravity. Thus, even though the $\mu_{||}$ method does not account for SRP, a 10% or better error in mass estimation is still expected to be achieved. If for any reason a 10% accuracy cannot be achieved with the nominal flyby plan presented here, more flybys can be added as needed to increase the estimation accuracy. Further, flybys can be planned with varying angles with respect to the sun in order to help isolate the effects of solar radiation pressure. Figure 10 shows the expected estimation error as a function of V_∞ and b_p for the nominal HO_3 density case; the flyby values are also marked in the figure.

The main measurement types for the $\mu_{||}$ method are the true anomaly angle and flyby time. The time-counting error is considered negligible in the time scales presented, and thus the true anomaly error is the main source of measurement error. This error is based on the accuracy of the measured pointing vector between spacecraft and asteroid and is defined as $\sigma_\nu = 10^{-4}$ rad. The initial state of each

flyby and the periape crossing distance estimation errors are also assumed to be negligible based on orbit determination schemes standard for deep space missions.

E. Instrument Selection

1. Optical Imaging Versus Lidar Versus Radar

Remote sensing instruments are either considered to be active or passive sensors, depending on whether or not they carry their own illumination source. Two major types of *active* sensors with flight heritage are available: radars and lidars. Radars operate over a large frequency band in the RF spectrum ranging from 3 MHz up to 300 GHz. Synthetic Aperture Radar (SAR) is the method of choice for reconstructing topography from a varying observation geometry, and has been in particular used by the Cassini mission to image the surface of Saturn's moon Titan [34]. However, typical SAR power requirements are nearly an order of magnitude beyond what can be provided by the NEACO spacecraft given the mission constraints. In addition, the necessary matching between a SAR's antenna dimensions and its operating wavelength makes integration on board of a volume- and mass-limited SmallSat spacecraft extremely challenging. It is also worth noting that the SAR data products require intense processing before they can be used.

Contrary to radar, lidar operates around the optical region of the RF spectrum. To date, only three major missions (Hayabusa-1, Hayabusa-2, and OSIRIS-REx) carried a lidar in their instrument suite, operating at 1064 nm [17]. They produce discrete point clouds representative of the topography of the observed scene. Because of their higher position in the RF spectrum, they have much smaller dimensions than radar systems and are also nearly insensitive to relative motion between the image shape and the instrument [35].

Lidars also have limiting factors. First, they require significant amounts of power to operate. The GoldenEye flash lidar and OLA scanning lidar on board OSIRIS-REx require, respectively, 50 and 60 W [35,36]. Second, current lidar can operate up to ranges around 10 km due to the reflected power falling under detection thresholds. In addition, reflected power and hence operating range will most likely be further reduced because of the low albedos typical for planetary bodies such as asteroids [37].

Although it is possible to use a lidar in this mission by hovering below 10 km, other instruments are able to perform more functions in the overall mission plan, outside of the 10 km envelope. Having instruments that can perform multiple functions is more important for mass- and volume-limited SmallSat missions. Further, using a lidar for global surface mapping would require a greater amount of science operations to occur at lower altitudes that are not as operationally safe. In contrast, passive optical instruments such as the AMICA and proposed NAC can fulfill science goals and navigational functions from much greater distances than lidar sensors. They also have lower volume, mass, and power requirements than both radar and lidar instruments, and are lower-risk systems due to their flight heritage.

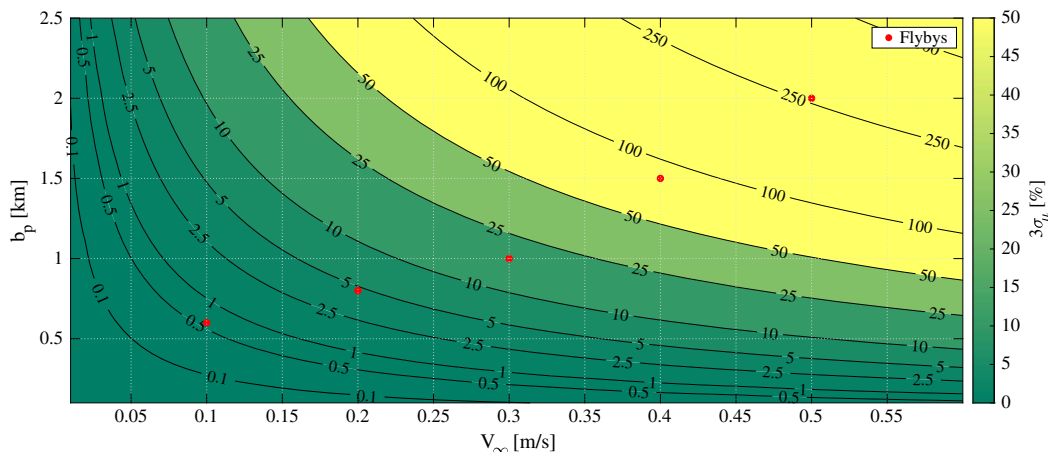


Fig. 10 $\mu_{||}$ estimation errors.

For these reasons, the baseline mission uses optical cameras without the addition of a radar or flash/scanning lidar.

2. Optical Imaging and Analysis

One of the main driving requirements in the optical imaging instrument selection is the instantaneous field of view (IFOV). This parameter dictates the distance at which a given instrument can meet the various resolution requirements necessary to achieve the stated science goals. A wide array of instruments were considered as candidates for inclusion in the NEACO mission concept. Plots similar to Fig. 5 were generated with candidate cameras to allow iterative selection as the science orbit selection and payload mass were narrowed down. The NAC IFOV was selected to allow operational and scientific goals to be met from relatively safe altitudes. The NAC IFOV satisfies the required resolutions of 1 m/px and 1 cm/px at altitudes, respectively, of 50 km and 600 m, as opposed to the 10 km and 100 m altitudes required for the AMICA camera that serves as a backup.

Given that so many science goals and operational needs are met using an optical camera, the inclusion of multiple cameras is required for redundancy purposes. Because the NAC has significant mass and volume requirements due to its large focal length and aperture, the smaller AMICA camera with a wider FOV was selected as the secondary camera. The AMICA, flown on the Hayabusa-1 spacecraft, is able to satisfy the mission goals in the event of a NAC failure. In nominal mission operations, AMICA's wider FOV may help contextualize NAC images of HO₃ at altitudes lower than 3 km, where the asteroid fills NAC's field of view. AMICA also has a filter wheel that may provide regional spectral information of the surface, though its spectral resolution is far lower than the Argus spectrometer.

Resolved images of HO₃'s surface collected by the cameras will be processed by means of stereophotoclinometry (SPC) to generate a shape model of the asteroid. Provided with an arbitrary large number of overlapping optical images, SPC produces an ensemble of landmark maps (L-maps) that are small digital albedo and elevation maps. Each L-map is thus a three-dimensional "tile" of the small body's surface [38]. These L-maps can then be used as navigation features or as the building blocks for a Global Topography Model (GTM). SPC is very robust to varying lighting conditions, image resolution, and angular separation. For instance, the Rosetta team reported a compatibility of SPC with surface-normal-to-camera angles (emission angles) up to 85° and phase angles ranging from nearly 0° to 160° [39]. This method is thus suitable to an iterative reconstruction of HO₃'s shape.

3. Altimeter

A laser altimeter similar to the instrument flown on board Hayabusa-1 is included in the NEACO instrument package to aid in both navigational and scientific tasks. First, the determination of HO₃'s gravitational parameter is dependent upon knowledge of the spacecraft state along the fly-by trajectory. As discussed in Sec. III.D, the reconstruction of this trajectory can be greatly improved if range measurements are available in complement with shape-model-based optical navigation techniques (OpNav). Second, the reconstructed shape model as well as the OpNav solution are only known up to a scaling factor. That is, the shape size and the separation between the imager and the shape are mutually indistinguishable. For large bodies such as Eros, the gravitational attraction is sufficiently large enough to make this scaling factor observable in Doppler measurements when the spacecraft is undergoing ordinary orbital motion [38]. For smaller bodies like Itokawa, specific free-fall Doppler-tracked trajectories must be instantiated in order to recover the scaling factor. For even smaller bodies like HO₃, it is likely that this would be even harder to schedule and accomplish. On the other hand, an altimeter would provide an unambiguous range measurement regardless of the orbital regime or the potential perturbations caused by maneuvers. In addition, contingencies arising during the proximity operations (such as imminent impact or escape) could be more easily detected and dealt with the altimeter than without.

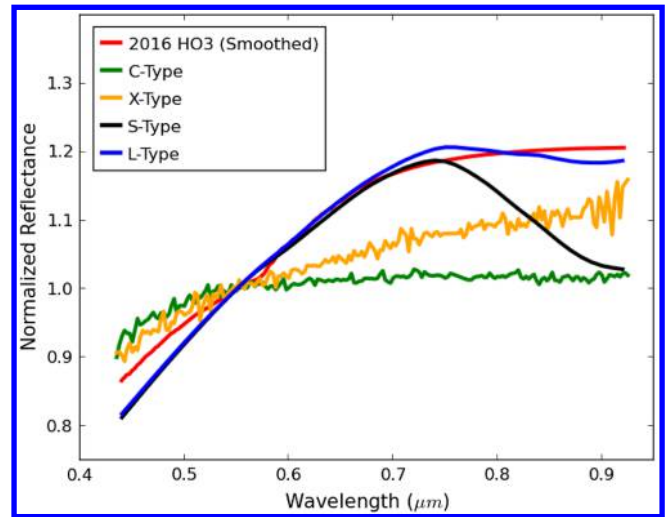


Fig. 11 Spectra of 2016 HO₃ compared with spectra types by Reddy et al. [3].

4. Spectrometer

Recently, Reddy et al. have classified 2016 HO₃ as an L-type asteroid by using ground-based observations of the asteroid [3]. Figure 11, produced by Reddy, shows the spectra of HO₃ as compared with the signatures of various asteroid types. L-type asteroids are sometimes confounded with S-type because they produce very similar spectral profiles. However, L-type asteroids have flatter spectra in the infrared region than S-type asteroids. Takahashi et al. describe the L-type as having a steep slope in the visible red region followed by a flat feature in the near infrared [40]. Thus, it is important that both the wavelengths in the visible region of the spectrum as well as the wavelengths in the near infrared region are considered when studying 2016 HO₃.

In particular, L-type asteroid spectra level out at 700 nm and show a slight concavity that produces a maximum at about 1500 nm [41]. There also may be a 2000 nm absorption band [41]. To characterize the entirety of 2016 HO₃'s spectral behavior, NEACO will have two spectrometers. The first spectrometer, the SWIS, will cover the visible spectrum and the lower end of the near infrared with a spectral range from 350 to 1700 nm and a spectral resolution of 5.7 nm [16]. To see whether the last absorption band exists at 2000 nm, NEACO will have an additional spectrometer, the Argus Space Grade Spectrometer, which has a spectral range from 1000 to 2500 nm and a spectral resolution of 6 nm [42]. With these two instruments, NEACO will be able to properly assess the spectra of 2016 HO₃ to help determine its composition.

F. ADCS Package Selection

The attitude control requirements considered in this study are derived from preliminary analysis of acceptable levels of motion blur with optical imaging cameras. The Blue Canyon Technologies FlexCore ADCS package was selected because it can provide the necessary control authority. To determine the acceptable levels of blur, the spacecraft is first assumed to have a nonzero angular drift ω_D rate about the asteroid spin axis ω_T . The relative attitude setup for this one-dimensional representation is visualized in Fig. 12. It shows a simplified pinhole camera at a distance r from the target. The target is modeled as a rotating rod of length D_T . This low-fidelity model helps determining a worst-case scenario in terms of relative motion.

Over a short time interval δt , a point initially aligned with the line of sight drifts by Δ :

$$\Delta \simeq \delta t \left(\omega_T \frac{D_T}{2} + \omega_D r \right) \quad (12)$$

In the vicinity of HO₃, exposure times around 1 s have an SNR orders of magnitude above the detection threshold of $S/N = 5$ (see Sec. V.B). Over such a short time, the approximations used in this

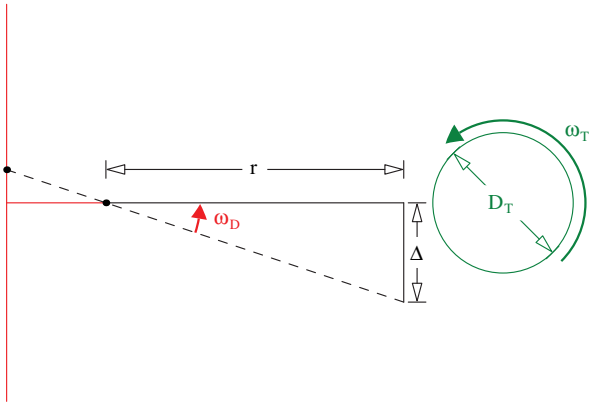


Fig. 12 Illustration of relative attitude components used to determine pointing requirements.

derivation remain valid. Zero motion blur is achieved when the displacement Δ is exactly zero. That is, $\omega_D^* = -(\omega_T D_T / 2r)$. The two drift rates exactly equating the maximum allowable drift rate are $\omega_{D,+} = \omega_D^* + (\Delta / r \Delta t)$ and $\omega_{D,-} = \omega_D^* - (\Delta / r \Delta t)$. To satisfy the lit surface mapping requirements, $\Delta < 1$ m must be true. The objective is to meet this requirement during the $r = 45$ km altitude hovering phase. As a result, the maximum allowable angular velocity drift for the 1 m resolution over 1 s is

$$\begin{aligned} \Delta \omega_{\max} &= \frac{\omega_{D,+} - \omega_{D,-}}{2} = \frac{\Delta}{r \Delta t} = 2.22 \cdot 10^{-5} \text{ rad/s} \\ &= 0.0013 \text{ deg/s} = 4.68 \text{ arcsec/s} \end{aligned} \quad (13)$$

The Blue Canyon XB Microsat package's pointing stability is rated at ± 1 arcsec/s [24]. Because this preceding analysis was conducted for a worst-case scenario where the angular displacement is maximum, this ADCS package appears to suit the needs of the mission. A more detailed analysis would need to account for wheel saturation and coupling between attitude knowledge and the attitude control system over all mission phases.

The nominal slew rate, which sets $\Delta = 0$, evaluates to $|\omega_D^*| = 2.08 \cdot 10^{-6} \text{ rad/s} = 0.00012 \text{ deg/s} = 0.43 \text{ arcsec/s}$. Because the torque discretization of the reaction wheels is limited, the pulsed plasma thrusters could be used to achieve this extremely low rotation rate. However, the nominal slew rate is an order of magnitude smaller than $\Delta \omega_{\max}$, and so a nominal slew rate of $\omega_D^* = 0$ is acceptable here. In a flyby trajectory, the nominal slew rate will be much greater to compensate for the relative motion.

G. Cohesive Strength Characterization

The measurement of an asteroid's strength provides scientific insight at several levels. First, planetary accretion in the early solar system occurred through the collision of planetesimal bodies; asteroids are thought to be remnants of this primordial planetesimal population [43]. Measurements of their strength may therefore improve general scientific understanding of the accretion processes that dominated the early solar system. Second, the design robustness of a kinetic impactor for planetary defense purposes is improved with accurate knowledge of its target's internal structure and strength [44,45]. Finally, methods to extract resources from asteroids, which have the potential to significantly decrease the cost of spaceflight, must be tuned toward the surface properties of their target [46].

When discussing asteroid strength, a distinction is made between the tensile, compressive, and cohesive strength of a body. First, the tensile strength of a body refers to its resistance to tensile forces and manifests itself mostly through the size and slope of overhangs on the asteroid surface. By examining cracks and cliffs with landslides, the tensile strength of a surface can be estimated. This was done for comet 67P/C-G during the Rosetta mission [47]. Because of its small size, asteroid HO₃ is likely a monolithic object, such that precise measurements of its tensile strength are improbable. At best, a lower

bound on the tensile strength can be constructed from accurate gravity, shape, and rotation models by estimating the internal stresses in the asteroid, which result primarily from its fast rotation rate. Second, the compressive strength of a body represents its resistance to compressive forces, which can be measured by penetrating or breaking the asteroid surface. This would either require a device that can be anchored to the asteroid surface or that impacts the surface at high velocity. Such devices are overly complex for the size of the NEACO spacecraft and are thus discarded. Finally, the cohesive strength refers to Van der Waals forces between small grains that make up the unconsolidated regolith found on many asteroids and comets [48]. Although the net gravitational and centrifugal acceleration points outward across almost all of the asteroid's surface, cohesion is theorized to allow for the existence of regolith across most of the asteroid, in particular at high latitudes above 60 deg. Using the methodology of Sánchez and Scheeres [9], a regolith layer of 10 cm requires only weak cohesion of approximately 0.02 Pa to exist, despite the fast rotation rate of HO₃. This holds for regolith particles as large as 3 mm, assuming the Hamaker constant of lunar regolith. Although Sánchez and Scheeres show that regolith may globally exist across the surface of a superfast rotator, it is most likely to exist near the asteroid poles, at latitudes greater than 60 deg. By examining the visual and spectral data of the asteroid surface, it will be possible to determine what, if any, regions of the asteroid have a regolith covering. More specifically, it holds that small regolith particles have distinctly different reflective properties than monolithic rock [10]. By determining the border between regolith-covered and regolith-free regions and estimating the accelerations in these regions, it is possible to constrain the magnitude of the cohesive forces.

Once the existence of regolith has been established, the estimate of the cohesive force magnitude will be further refined using a small impactor. Although the impactor could be released while the mothership descends toward the asteroid surface at high velocity (several m/s) to minimize the effect of navigation uncertainties, this would require sufficient thrust to execute a braking maneuver. Given the limited thrust level of the XiPS and μ CAT thrusters, this is not possible. A similar argument can be made against using a detachable explosive impactor, which would require the spacecraft to quickly evacuate to the opposite face of the asteroid before detonation. Instead, the NEACO mission concept proposes to use a low-velocity impactor that is released during hovering at a very low altitude. In this process the spacecraft maintains some altitude h above the asteroid surface with vertical position error σ_h and horizontal position error σ_x . The impactor is then ejected via a spring mechanism at some velocity ΔV in direction θ . This is an established technique that is also used by the Hayabusa2 spacecraft to deploy the MINERVA-II (Micro Nano Experimental Robot Vehicle for Asteroid, the second generation) rovers and the Mobile Asteroid Surface Scout (MASCOT) lander to asteroid Ryugu [49]. The mentioned parameters are illustrated in Fig. 13.

The impactor deployment is challenging: given that the impactor is fully passive, it must be released in a way that guarantees surface

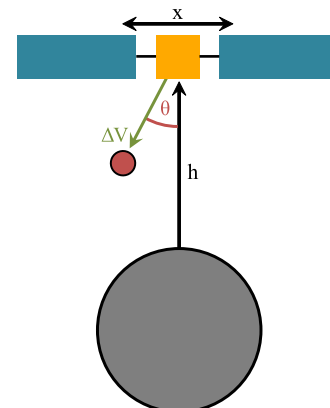


Fig. 13 Illustration of the impactor release geometry during low-altitude hovering.

impact in the presence of navigation and release uncertainties, despite the asteroid's small size. A detailed covariance analysis of the achievable on-board navigation accuracies is considered beyond the scope of this proposal paper. Nevertheless, it is important to estimate the level of guidance, navigation, and control (GNC) precision required for successful impactor release. Subsequent study may then determine what additional system design and on-board processing is required to achieve this precision.

During the low-altitude hovering before impactor release, the spacecraft uses its altimeter to estimate its altitude and vertical velocity. Because of the precision of this instrument and the pulsed plasma thrusters, vertical control can be performed with appreciable precision. The horizontal position and velocity estimation is expected to be far more challenging, as this must be obtained from either on-board surface-relative navigation and/or using some one-way signal from Earth (e.g., a Doppler range-rate measurement). In simple tests performed for this study, velocity uncertainties have been found to be the most critical parameters in guaranteeing successful impact. The horizontal and vertical position errors are therefore both fixed at $\sigma_x = \sigma_h = 1$ m in order to focus on variations in the velocity errors. The NEACO impactor release mechanism mimics the design of the Mechanical and Electrical Support System (MESS) that houses and releases the MASCOT lander on the Hayabusa2 spacecraft [50]. This mechanism has a spring velocity error of $\sigma_{\Delta V} = 10\%$ and $\sigma_\theta = 1.7$ deg on the release of MASCOT. Both the release velocity magnitude ΔV and the horizontal velocity error σ_{vx} are then varied to test for the rate of successful deployment, at various hovering altitudes. As an example, Fig. 14 shows examples of successful and unsuccessful deployment at an altitude of 100 m. Note that, due to the weak gravitational attraction of HO₃, the probe trajectories are effectively straight lines. As a result, the deployment success is independent of the particular value of μ , when it varies within the previously stated bounds.

The deployment success for different sets of (V_0, σ_{vx}) at altitudes of $h = [50, 100, 250]$ m has been investigated in this study. From this analysis, the release from $h = 100$ m provides the best combination of deployment success and spacecraft safety. Table 9 provides the corresponding success rates for different sets of (V_0, σ_{vx}) for the $h = 100$ m scenario. The results show a clear trade-off between V_0 and σ_{vx} ; if the release velocity is higher, a larger horizontal velocity error is acceptable.

The results in this table show that release can indeed be achieved with realistic navigation precision from an altitude of $h = 100$ m. With a release velocity of $V_0 = 1.0$ m/s, the probe impact is successful if the horizontal velocity precision σ_{vx} is better than 5 cm/s.

Table 9 Deployment success rate from $h = 100$ m (4R)

	σ_{vx} , m/s			
V_0 , m/s	0.05	0.10	0.15	0.30
0.50	99.8%	95.0%	68.1%	40.0%
0.75	99.9%	99.5%	85.7%	55.3%
1.00	100%	99.8%	94.3%	67.4%
1.25	100%	99.9%	97.7%	77.8%

These results provide an order-of-magnitude estimate of the release and horizontal velocity requirements for successful impactor delivery. Further study with navigation signal modeling is necessary to determine whether this delivery is indeed feasible for NEACO.

The system design of the MASCOT lander on board Hayabusa2 is used to estimate the mass of the NEACO impactor system. The MASCOT lander has a total mass of 10 kg, which is housed in the mothership and released from it by the MESS, which has an additional mass of 5 kg [50]. Using a conservative estimate for NEACO's low-velocity impactor of 1 kg, and the ratio of MASCOT lander mass to MESS mass, the total mass of the NEACO impactor and its housing/release structure is estimated to be 1.5 kg.

VI. Conclusions

The Near-Earth Asteroid Characterization and Observation (NEACO) mission concept proposes to perform an elementary investigation of asteroid 2016 HO₃ using a single SmallSat spacecraft that travels to HO₃ using a low-thrust SEP transfer trajectory. Pulsed plasma thrusters allow for hovering and maneuvering in proximity of the asteroid. The spacecraft is equipped with two optical cameras, two spectrometers, a laser altimeter, and an impactor assembly. This instrument suite allows NEACO to resolve the asteroid shape, estimate its mass, perform mapping and spectroscopy of the surface, and measure the strength of this small, fast-rotating, near-Earth asteroid.

The NEACO mission concept study has demonstrated that a SmallSat mission to a near-Earth asteroid is not only feasible, but also can return significant scientific information about the asteroid. This information can inform the design of future, larger-scale missions to HO₃. This study has also illuminated some of the difficulties in accomplishing such a mission to a small body, along with proposed methods to address these issues. Major challenges that were addressed include finding an adequate interplanetary trajectory with SmallSat limitations, finding safe scientific orbits close enough to HO₃ to accomplish science goals, estimating the mass of such a small body

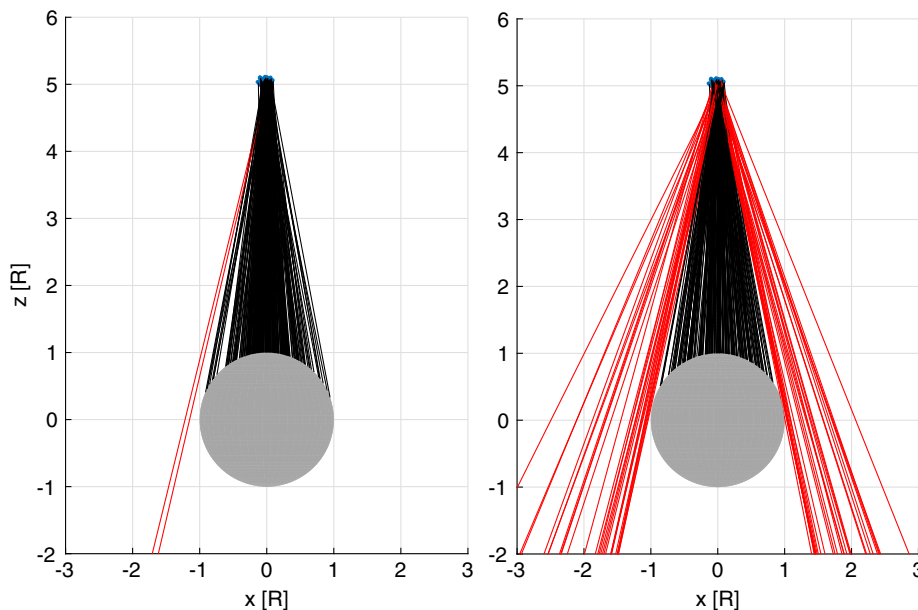


Fig. 14 Impactor release with $h = 100$ m, $V_0 = 1.25$ m/s, and (left) $\sigma_{vx} = 0.10$ m/s and (right) $\sigma_{vx} = 0.20$ m/s.

with a SmallSat, and characterizing the asteroid surface strength with an impactor. The preliminary investigations found here are excellent starting points for deeper investigation into specific aspects of the overall mission design. Further, the combination of analyses here can serve as a reference for other mission designs to other small bodies using SmallSats.

Acknowledgments

Special thanks to São Paulo State University Ph.D. students and NEACO team members Josué Cardoso dos Santos and Gabriel Borderes-Motta for their help on this project. Alex Davis, Conor Benson, and Nathan Parrish (while still a student) were also valuable NEACO team members. Thanks to Ann Dietrich, Jacob Englander, Masatoshi Hirabayashi, Jason Leonard, Jay McMahon, Daniel Scheeres, and Simon Tardivel for consulting with our team and giving general advice.

References

- [1] de la Fuente Marcos, C., and de la Fuente Marcos, R., "Asteroid (469219) 2016 HO₃, the Smallest and Closest Earth Quasi-Satellite," *Monthly Notices of the Royal Astronomical Society*, Vol. 462, No. 4, 2016, pp. 3441–3456.
doi:10.1093/mnras/stw1972
- [2] Perna, D., Barucci, M. A., and Fulchignoni, M., "The Near-Earth Objects and Their Potential Threat to Our Planet," *The Astronomy and Astrophysics Review*, Vol. 21, No. 1, 2013, p. 65.
doi:10.1007/s00159-013-0065-4
- [3] Reddy, V., Kuhn, O., Thirouin, A., Mommert, M., Conrad, A., Malhotra, R., Sanchez, J., and Veillet, C., "Ground-Based Characterization of Earth Quasi Satellite 2016 HO₃," *Division for Planetary Sciences of the American Astronomical Society*, American Astronomical Soc. Paper 204.07, Washington, D.C., 2017.
- [4] Venigalla, C., Baresi, N., Aziz, J., Bercovici, B., Borderes Motta, G., Brack, D., Cardoso dos Santos, J., Dahir, A., Davis, A. B., Smet, S. D., et al., "The Near-Earth Asteroid Characterization and Observation (NEACO) Mission," *Advances in the Astronautical Sciences*, AAS Paper 17-744, Springfield, VA, 2017, pp. 3543–3576.
- [5] Hughes, S. P., Qureshi, R. H., Cooley, D. S., Parker, J. J. K., and Grubb, T. G., "Verification and Validation of the General Mission Analysis Tool (GMAT)," *AIAA/AAS Astrodynamics Specialist Conference*, AIAA, Reston, VA, Aug. 2014.
doi:10.2514/6.2014-4151
- [6] Yeomans, D. K., Antreasian, P. G., Cheng, A., Dunham, D. W., Farquhar, R. W., Gaskell, R. W., Giorgini, J. D., Helfrich, C. E., Konopliv, A. S., McAdams, J. V., et al., "Estimating the Mass of Asteroid 433 Eros During the NEAR Spacecraft Flyby," *Science*, Vol. 285, No. 5427, 1999, pp. 560–561.
doi:10.1126/science.285.5427.560
- [7] Broschart, S., Bhaskaran, S., Bellerose, J., Dietrich, A., HAN, D., HAW, R., Mastrodemos, N., Owen, W., RUsh, B., and Surovik, D., "Shadow Navigation Support at JPL for the Rosetta Landing on Comet 67P," *26th International Symposium on Space Flight Dynamics*, Japan Aerospace Exploration Agency Paper ISSFD-2017-096, Matsuyama, 2017.
- [8] Jackman, C. D., Nelson, D. S., McCarthy, L. K., Finley, T. J., Liounis, A. J., Getzandanner, K. M., Antreasian, P. G., and Moreau, M. C., "Optical Navigation Concept of Operations for the OSIRIS-REX Mission," *Spaceflight Mechanics 2017, PTS I–IV*, Vol. 160, Feb. 2017, pp. 3337–3354.
- [9] Sánchez Lana, D. P., and Scheeres, D. J., "Regolith on Super Fast Rotators," *AAS/Division for Planetary Sciences Meeting Abstracts*, Vol. 49, Oct. 2017, p. 204.11.
- [10] Adams, J. B., and Filice, A. L., "Spectral Reflectance 0.4 to 2.0 Microns of Silicate Rock Powders," *Journal of Geophysical Research*, Vol. 72, No. 22, 1967, pp. 5705–5715.
doi:10.1029/JZ072i022p05705
- [11] Van Wal, S., Tardivel, S., and Scheeres, D., "Parametric Study of Ballistic Lander Deployment to Small Bodies," *Journal of Spacecraft and Rockets*, Vol. 54, No. 6, Nov. 2017, pp. 1–26.
doi:10.2514/1.A33832
- [12] Keller, H. U., Barbieri, C., Lamy, P., Rickman, H., Rodrigo, R., Wenzel, K.-P., Sierks, H., A'Hearn, M. F., Angrilli, F., Angulo, M., et al., "OSIRIS—The Scientific Camera System Onboard Rosetta," *Space Science Reviews*, Vol. 128, No. 1, 2007, pp. 433–506.
doi:10.1007/s11214-006-9128-4
- [13] Jin, H., Lim, J., Kim, Y., and Kim, S., "Optical Design of a Reflecting Telescope for Cubesat," *Journal of the Optical Society of Korea*, Vol. 17, No. 6, 2013, pp. 533–537.
doi:10.3807/JOSK.2013.17.6.533
- [14] Bosanac, N., Do, S., Wen, H. Y., and Wicht, A., "A General Purpose Astronomy Small Satellite: An approach to Low-Cost Space Telescope Design Using Space-Qualified Ground Telescopes," *Proceedings of SPIE 7731, Space Telescopes and Instrumentation 2010: Optical, Infrared, and Millimeter Wave*, Aug. 2010, Paper 7731.
doi:10.1117/12.858018
- [15] Ishiguro, M., Nakamura, R., Tholen, D. J., Hirata, N., Demura, H., Nemoto, E., Nakamura, A. M., Higuchi, Y., Sogame, A., Yamamoto, A., et al., "The Hayabusa Spacecraft Asteroid Multi-Band Imaging Camera: AMICA," *Icarus*, Vol. 207, No. 2, 2010, pp. 714–731.
doi:10.1016/j.icarus.2009.12.035
- [16] Bender, H. A., Mouroulis, P., Smith, C. D., Smith, C. H., Van Gorp, B. E., Eastwood, M. L., and Gross, J., "Snow and Water Imaging Spectrometer (SWIS): Optomechanical and System Design for a CubeSat-Compatible Instrument," *Imaging Spectrometry XX*, Vol. 9611, International Soc. for Optics and Photonics, Bellingham, WA, 2015, Paper 961103.
doi:10.1117/12.2190013
- [17] Tsuno, K., Okumura, E., Katsuyama, Y., Mizuno, T., Hashimoto, T., Nakayama, M., and Yuasa, H., "Lidar on Board Asteroid Explorer Hayabusa," *Proceedings of SPIE 10567, International Conference on Space Optics—ICSO 2006*, Nov. 2017, Paper 105670W.
doi:10.1117/12.2308048
- [18] Mukai, T., Araki, H., Mizuno, T., Hatanaka, N., Nakamura, A., Kamei, A., Nakayama, H., and Cheng, A., "Detection of Mass, Shape and Surface Roughness of Target Asteroid of MUSES-C by LIDAR," *Advances in Space Research*, Vol. 29, No. 8, 2002, pp. 1231–1235.
doi:10.1016/S0273-1177(02)00141-2
- [19] Tighe, W. G., Chien, K., Ahn, J., Hurtado, J., Solis, E., and Spears, R., "Update on the XIPS 8-cm Thruster Prototype," *44th AIAA/ASME/SAE/ASEE Joint Propulsion Conference & Exhibit*, AIAA Paper 2008-4912, 2008.
doi:10.2514/6.2008-4912
- [20] Manzella, D., "Low Cost Electric Propulsion Thruster for Deep Space Robotic Missions," *2007 NASA Science Technology Conference*, NASA TM-2008-215067, E-16288, 2007, https://esto.nasa.gov/conferences/nstc2007/papers/Manzella_David_D10P2_NSTC-07-0116.pdf.
- [21] Tighe, W., Chien, K., and Spears, R., "XIPS Ion Thrusters for Small Satellite Applications," *21st Annual AIAA/USU Conference on Small Satellites, SC07-III-11*, American Inst. of Aeronautics and Astronautics (AIAA) and Utah State Univ. (USU) Paper SSC07-III-11, 2007, <http://digitalcommons.usu.edu/cgi/viewcontent.cgi?article=1459&context=smallsat>.
- [22] Agasid, E., Burton, R., Carlino, R., Defouw, G., et al., "Small Spacecraft Technology State of the Art," NASA TP–2015, 2015.
- [23] McGuire, M. L., and Myers, R. M., "Pulsed Plasma Thrusters for Small Spacecraft Attitude Control," NASA CR 198517, Aug. 1996.
- [24] "XB Spacecraft," Tech. Rept., Blue Canyon Technologies, 2018, http://bluecanyontech.com/wp-content/uploads/2018/01/DataSheet_XBspacecraft_11_F.pdf, [accessed 4 April 2018].
- [25] "FlexCore—XACT Attitude Control Scalable to Microsatellites," Tech. Rept., Blue Canyon Technologies, 2018, http://bluecanyontech.com/wp-content/uploads/2017/03/DataSheet_Flexcore_05.pdf, [accessed 4 April 2018].
- [26] Englander, J. A., and Conway, B. A., "Automated Solution of the Low-Thrust Interplanetary Trajectory Problem," *Journal of Guidance, Control, and Dynamics*, Vol. 40, No. 1, 2017, pp. 15–27.
doi:10.2514/1.G002124
- [27] Muinonen, K., Belskaya, I. N., Cellino, A., Delbò, M., Levasseur-Regourd, A.-C., Penttilä, A., and Tedesco, E. F., "A Three-Parameter Magnitude Phase Function for Asteroids," *Icarus*, Vol. 209, No. 2, 2010, pp. 542–555.
doi:10.1016/j.icarus.2010.04.003
- [28] Photometrics, "Keep the Noise Down! Low Noise: An Integral Part of High-Performance CCD (HCCD) Camera Systems," Photometrics Tech. Rept. A1, Tucson, AZ, 2010, <https://www.photometrics.com/resources/technotes/pdfs/snr.pdf>.
- [29] Barbieri, C., Fornasier, S., Bertini, I., Angrilli, F., Bianchini, G., Debei, S., De Cecco, M., Parzianello, G., Zaccariotto, M., Da Deppo, V., et al., "First Results from the Wide Angle Camera of the ROSETTA Mission," *Memorie della Società Astronomica Italiana Supplementi*, Vol. 6, Jan. 2005, p. 28.
- [30] Scheeres, D. J., and Marzari, F., "Spacecraft Dynamics in the Vicinity of a Comet," *Journal of the Astronautical Sciences*, Vol. 50, No. 1, 2002, pp. 35–52.

- [31] Scheeres, D. J., *Orbital Motion in Strongly Perturbed Environments*, Springer-Verlag, Berlin, 2012, Chap. 13. doi:10.1007/978-3-642-03256-1
- [32] Kikuchi, S., Howell, K. C., Tsuda, Y., and Kawaguchi, J., "Orbit-Attitude Coupled Motion Around Small Bodies: Sun-Synchronous Orbits with Sun-Tracking Attitude Motion," *Acta Astronautica*, Vol. 140, Nov. 2017, pp. 34–48. doi:10.1016/j.actaastro.2017.07.043
- [33] Takahashi, Y., and Scheeres, D. J., "Small-Body Postrendezvous Characterization via Slow Hyperbolic Flybys," *Journal of Guidance, Control and Dynamics*, Vol. 34, No. 6, 2011, pp. 1815–1827. doi:10.2514/1.53722
- [34] Elachi, C., Wall, S., Allison, M., Anderson, Y., Boehmer, R., Callahan, P., Encrenaz, P., Flamini, E., Franceschetti, G., Gim, Y., et al., "Cassini Radar Views the Surface of Titan," *Science*, Vol. 308, No. 5724, 2005, pp. 970–974. doi:10.1126/science.1109919
- [35] Daly, M. G., Barnouin, O. S., Dickinson, C., Seabrook, J., Johnson, C. L., Cunningham, G., Haltigin, T., Gaudreau, D., Brunet, C., Aslam, I., et al., "The OSIRIS-REx Laser Altimeter (OLA) Investigation and Instrument," *Space Science Reviews*, Vol. 212, No. 1, Oct. 2017, pp. 899–924. doi:10.1007/s11214-017-0375-3
- [36] Advanced Scientific Concepts, "GoldenEye 3D Flash LIDAR™ Space Camera," 2018, <http://www.advancedscientificconcepts.com/products/portable.html>, [accessed 4 April 2018].
- [37] Shevchenko, V. G., and Tedesco, E. F., "Asteroid Albedos Deduced from Stellar Occultations," *Icarus*, Vol. 184, No. 1, 2006, pp. 211–220. doi:10.1016/j.icarus.2006.04.006
- [38] Gaskell, R. W., Barnouin-Jha, O. S., Scheeres, D. J., Konopliv, a. S., Mukai, T., Abe, S., Saito, J., Ishiguro, M., Kubota, T., Hashimoto, T., et al., "Characterizing and Navigating Small Bodies with Imaging Data," *Meteoritics and Planetary Science*, Vol. 43, No. 6, 2008, pp. 1049–1061. doi:10.1111/maps.2008.43.issue-6
- [39] Castellini, F., Santayana, R. P. D., Vantournhout, K., and Lauer, M., "Operational Experience and Assessment of the Implementation of the Maplet Technique for Rosetta's Optical Navigation," *AAS/AIAA Astrodynamics Specialist Conference*, AAS Paper 17-718, Springfield, VA, 2017, pp. 1–20.
- [40] Takahashi, J., Urakawa, S., Terai, T., Hanayama, H., Arai, A., Honda, S., Takagi, Y., Itoh, Y., Zenno, T., and Ishiguro, M., "Near-Infrared Colors of Asteroid 2012 DA14 at its Closest Approach to Earth: Observations with the Nishiharima Infrared Camera (NIC)," *Publications of the Astronomical Society of Japan*, Vol. 66, No. 3, 2014, p. 53. doi:10.1093/pasj/psu042
- [41] DeMeo, F. E., Binzel, R. P., Slivan, S. M., and Bus, S. J., "An Extension of the Bus Asteroid Taxonomy into the Near-Infrared," *Icarus*, Vol. 202, No. 1, 2009, pp. 160–180. doi:10.1016/j.icarus.2009.02.005
- [42] "Argus IR Spectrometer Kit, Space Grade," Tech. Rept., Thoth Technologies, 2018, <http://thothx.com/product/argus-1000sk-infrared-spectrometer-kit/>, [accessed 4 April 2018].
- [43] Saiki, T., Sawada, H., Okamoto, C., Yano, H., Takagi, Y., Akahoshi, Y., and Yoshikawa, M., "Small Carry-on Impactor of Hayabusa2 Mission," *Acta Astronautica*, Vol. 84, March 2013, pp. 227–236. doi:10.1016/j.actaastro.2012.11.010
- [44] Cheng, A., Michel, P., Jutzi, M., Rivkin, A., Stickle, A., Barnouin, O., Ernst, C., Atchison, J., Pravec, P., and Richardson, D., et al., "Asteroid Impact & Deflection Assessment Mission: Kinetic Impactor," *Planetary and Space Science*, Vol. 121, Feb. 2016, pp. 27–35. doi:10.1016/j.pss.2015.12.004
- [45] Stickle, A., Atchison, J., Barnouin, O., Cheng, A., Ernst, C., Fletcher, Z., Richardson, D., and Rivkin, A., "Modeling Momentum Transfer from the Dart Spacecraft Impact into the Moon of Didymos," *Proceedings of the 4th IAA Planetary Defense Conference*, International Academy of Astronautics Paper IAA-PDC-15-04-04, Frascati, Italy, 2015.
- [46] Sanchez, J., and McInnes, C., "Asteroid Resource Map for Near-Earth Space," *Journal of Spacecraft and Rockets*, Vol. 48, No. 1, 2011, pp. 153–165. doi:10.2514/1.49851
- [47] Groussin, O., Jorda, L., Auger, A.-T., Kührt, E., Gaskell, R., Capanna, C., Scholten, F., Preusker, F., Lamy, P., Hviid, S., et al., "Gravitational Slopes, Geomorphology, and Material Strengths of the Nucleus of Comet 67P/Churyumov-Gerasimenko from OSIRIS Observations," *Astronomy & Astrophysics*, Vol. 583, Oct. 2015, p. A32. doi:10.1051/0004-6361/201526379
- [48] Rozitis, B., MacLennan, E., and Emery, J. P., "Cohesive Forces Prevent the Rotational Breakup of Rubble-Pile Asteroid (29075) 1950 DA," *Nature*, Vol. 512, No. 7513, 2014, pp. 174–176. doi:10.1038/nature13632
- [49] Tsuda, Y., Yoshikawa, M., Abe, M., Minamino, H., and Nakazawa, S., "System Design of the Hayabusa 2—Asteroid Sample Return Mission to 1999 JU3," *Acta Astronautica*, Vol. 91, Oct. 2013, pp. 356–362. doi:10.1016/j.actaastro.2013.06.028
- [50] Ho, T., Biele, J., and Lange, C., "AIM MASCOT-2 Asteroid Lander Concept Design Assessment Study," *DLR Executive Summary v1.0*, DLR Inst. of Space Systems, 2016.

C. W. T. Roscoe
Associate Editor

This article has been cited by:

1. Christian Cenci, Andrea D'Ambrosio, Hanlun Lei, Emiliano Ortore. 2019. Global mapping of asteroids by frozen orbits: The case of 216 kleopatra. *Acta Astronautica* **161**, 101-107. [[Crossref](#)]